

Doctoral Dissertation

博士論文

Structural analysis of plant vacuolar iron transporter VIT1  
(植物の液胞膜鉄トランスポーターVIT1の構造解析)

A Dissertation Submitted for the Degree of Doctor  
of Philosophy

令和元年12月博士(理学)申請

March 2020

Department of Biological Sciences, Graduate School of Science,  
The University of Tokyo

東京大学大学院理学系研究科

生物科学専攻

Takafumi Kato

加藤 孝郁

## Abstract

Iron ion is one of the most essential cofactors in several vital enzymatic reactions, such as DNA replication and respiratory and photosynthetic electron transfer chains in all organisms. However, cytoplasmic excessive accumulation of iron ion induces reactive oxygen species which directly damage biomolecules in cells, and thus the concentration of iron ion is strictly regulated by various proteins and organelles. Iron ions are captured by iron-binding proteins and also transported by membrane proteins to keep its cytoplasmic concentration at low levels. In plant cells vacuoles play a key role in iron homeostasis, by isolating and storing iron ions. Vacuolar Iron Transporter 1 (VIT1) is essential for iron homeostasis in plants. VIT1 transports cytoplasmic  $\text{Fe}^{2+}$  into the vacuolar lumen, and overexpression of VIT1 leads to an increased iron accumulation in crops, which could be useful for the treatment of human iron deficiency diseases. In addition, a VIT1 homologue from the malaria-causing parasite *Plasmodium falciparum* is considered as a potential drug target for malaria. Therefore, it is important to understand the structure and the detailed molecular mechanism of VIT1. However, structural information of VIT1 has been unclear, because VIT1 does not share amino acid sequence similarity with other known transporters.

Here, I report the crystal structure and functional analysis of VIT1 from Rose Gum *Eucalyptus grandis* (EgVIT1). EgVIT1 functions as a  $\text{H}^+$ -coupled antiporter for  $\text{Fe}^{2+}$  and other transition metal ions. I determined two distinct structure of EgVIT1, and also determined the structure of the cytoplasmic domain, soaked in four different ions ( $\text{Zn}^{2+}$ ,  $\text{Ni}^{2+}$ ,  $\text{Co}^{2+}$  and  $\text{Fe}^{2+}$ ), using X-ray crystallography. VIT1 adopts a novel protein fold forming a dimer of five-membrane-spanning domains, with an ion-translocating pathway constituted by the conserved methionine and carboxylate residues at the dimer interface.

The second transmembrane helix protrudes from the lipid membrane by about 40 Å and connects to a three-helical-bundle triangular cytoplasmic domain, which binds to the substrate metal ions and stabilizes their soluble form, and thus playing an essential role in the transport. These mechanistic insights will provide useful information for the further design of genetically modified crops and the development of anti-malaria drugs.



# Contents

<b>Abstract</b> .....	2
<b>List of figures</b> .....	7
<b>List of tables</b> .....	12
<b>Abbreviations</b> .....	14
<b>Table of Amino Acid abbreviations</b> .....	18
<b>Chapter 1 General introduction</b> .....	19
<b>1-1 Basics of membrane transporter</b> .....	19
<b>1-1-1 Membrane transporters</b> .....	19
<b>1-2 Iron ion homeostasis</b> .....	23
<b>1-2-1 Iron ion as cofactor and toxin</b> .....	23
<b>1-2-2 Plant iron ion homeostasis</b> .....	23
<b>1-3 Vacuolar Iron Transporter 1 (VIT1)</b> .....	25
<b>1-3-1 Function of VIT1</b> .....	25
<b>1-3-2 Structural feature of VIT1</b> .....	25
<b>Chapter 2 Structural analysis of VIT1</b> .....	29
<b>2-1 Introduction</b> .....	29
<b>2-2 Materials and methods</b> .....	29
<b>2-2-1 Plasmid construction of VIT1 for crystallography</b> .....	29
<b>2-2-2 Expression and purification of VIT1 protein</b> .....	29
<b>2-2-3 Expression and purification of isolated MBD protein</b> .....	30
<b>2-2-4 Crystallization and structural determination of VIT1 protein</b> .....	31
<b>2-2-5 Crystallization and structural determination of isolated MBD</b> .....	33
<b>2-3 Result</b> .....	35
<b>2-3-1 Purification and crystallization of Eucalyptus grandis VIT1</b> .....	35
<b>2-3-2 Structural determination of EgVIT1</b> .....	37
<b>2-3-3 Overall structure of EgVIT1</b> .....	42
<b>Chapter 3 Transport mechanism of VIT1</b> .....	46
<b>3-1 Introduction</b> .....	46
<b>3-2 Materials and methods</b> .....	46
<b>3-2-1 Spot analyses (Fe<sup>2+</sup> sensitivity spot assay)</b> .....	46
<b>3-2-2 Preparation of proteolipomes</b> .....	47
<b>3-2-3 Liposomal assay</b> .....	47
<b>3-3 Result</b> .....	49
<b>3-3-1 EgVIT1 functions as H<sup>+</sup>-coupled antiporter</b> .....	49

<b>3-3-2 Ion transport pathway at transmembrane domain</b> .....	54
<b>3-3-3 Function of cytoplasmic metal binding domain</b> .....	59
<b>Chapter 4 General discussion</b> .....	70
<b>4-1 Introduction</b> .....	70
<b>4-2 H<sup>+</sup> coupled mechanism and metal ion recognition</b> .....	70
<b>4-3 Conformational change during transport</b> .....	75
<b>4-4 Function of MBD</b> .....	75
<b>4-5 Conclusion</b> .....	77
<b>4-6 Future perspective</b> .....	78
<b>Table 1</b> Data collection and refinement statistics for <i>EgVIT1</i> <sub>90-165</sub> .....	81
<b>Table 2</b> Data collection and refinement statistics for <i>EgVIT1</i> <sub>23-249</sub> .....	84
<b>Alignment</b> .....	87
<b>Reference</b> .....	91
<b>Original paper</b> .....	98
<b>Acknowledgment</b> .....	100

## **List of figures**

1.1 Membrane transporters

1.2 Substrate recognition

1.3 Kinds of transporters

1.4 Rocker-switch model

1.5 Vacuole isolates and stores iron ions

1.6 Predicted topology of VIT1

1.7 Cytoplasmic diversity among VIT1 family

2.1 Disorder prediction

2.2 Screening and thermostability of EgVIT1

2.3 Crystal of EgVIT1<sub>23-249</sub> and X-ray diffraction pattern

2.4 Alignment between EgVIT1 and AtVIT1

2.5 Crystal of EgVIT1<sub>23-249</sub> with Hg

2.6 Electron density of transmembrane and cytoplasmic regions

2.7 Crystal packing of EgVIT1<sub>23-249</sub>

2.8 Electron density of transmembrane and cytoplasmic regions

2.9 Crystal packing of EgVIT1<sub>23-249</sub>

2.10 Overall structure of EgVIT1

2.11 Clockwise order

2.12 Overview of asymmetric unit of MBD and hydrophobic interaction

3.1 Overall structure of EgVIT1

3.2 Clockwise order

3.3 Overview of asymmetric unit of MBD and hydrophobic interaction

3.4 pH has an influence on the transport activity of EgVIT1

3.5 CCCP decreases the transport activity of EgVIT1

3.6 Liposomal assay by proton indicator pyranine

3.7 EgVIT1 transports proton

3.8 Hydrophilic pocket at TMD

3.9 Transport activity of mutants of the hydrophilic pocket

3.10 Cobalt ion is coordinated by the hydrophilic pocket

3.11 Kink-induced residues

3.12 Measuring H<sup>+</sup> transport

3.13 Structure of MBD

3.14 Anomalous density of the zinc ion in EgVIT1<sub>23-249</sub>

3.15 Metal binding site at MBD

3.16 Anomalous difference densities of metal ions bound to MBD

3.17 Anomalous signal of nickel, cobalt and iron ion

3.18 Spot assay of mutants of the cytoplasmic metal binding site

3.19 Liposomal assay of mutants of the cytoplasmic metal binding site

3.20 Competition of zinc ion

3.21 Ion translocation from the MBD to TMD

4.1 Methionine residues of iron transporters

4.2 Co<sup>2+</sup> binding induces partial occlusion by Met80

4.3 Iron ion transport by the hydrophilic pocket at TMD

4.4 Putative function of MBD





## **List of tables**

Table 1 Data collection and refinement statistics for EgVIT1<sub>90-165</sub>

Table 2 Data collection and refinement statistics for EgVIT1<sub>23-249</sub>



## Abbreviations

OC..... OCcluded state

OF..... Outward-Facing state

IF..... Inward-Facing state

ROS..... Reactive Oxygen Species

VIT1..... Vacuolar Iron Transporter 1

CCC1..... Cross-Complements Ca<sup>2+</sup> phenotype of the *csg1*

VTLs..... Vacuolar iron transporter Like Transporters

MbfA..... membrane-bound ferritin A

EgVIT1..... *Eucalyptus grandis* VIT1

URA3..... URAcil requiring 3

TEV..... Tobacco Etch Virus

PEP4.....carboxyPEPTidase Y-deficient 4

YNB..... Yeast Nitrogen Base

CSM-Ura..... Complete Supplement Mixture minus Uracil

Tris..... Tris(hydroxymethyl)aminomethane

PMSF..... PhenylMethylSulfonyl Fluoride

DDM.....n-Dodecyl- $\beta$ -D-Maltoside

CSH..... Cholesteryl HemiSuccinate

SEC..... Size exclusion Chromatography

MWCO..... Molecular Weight Cut Off

SUMO..... Small Ubiquitin-related MODifier

OD..... Optical Density

IPTG..... IsoPropyl- $\beta$ -D-ThioGalactopyranoside

LCP..... Lipidic Cubic Phase

HEPES..... 4-(2-HydroxyEthyl)-1-PiperazineEthaneSulfonic acid

PEG..... PolyEthylene Glycol

DME..... Di-Methyl Ether

SPRING-8..... Super Photon ring-8 GeV

SIR..... single isomorphous replacement

SAD..... Single-wavelength Anomalous Diffraction

TMD..... TransMembrane Domain

MBD..... Metal Binding Domain

MES..... 2-(N-Morpholino)EthaneSulfonic acid

DM..... n-Decyl- $\beta$ -D-Maltoside

CCCP..... Carbonyl Cyanide m-ChloroPhenyl hydrazone

Met-mut..... Met double mutan

Glu-mut..... Glutamate five-fold mutant

DMT..... Divalent Metal Transporter

NRAMP..... Natural Resistance-Associated Macrophage Protein



**Table of Amino Acid abbreviations**

1 letter	3 letter	Full name	1 letter	3 letter	Full name
A	Ala	Alanine	M	Met	Methionine
C	Cys	Cysteine	N	Asn	Asparagine
D	Asp	Aspartate	P	Pro	Proline
E	Glu	Glutamate	Q	Gln	Glutamine
F	Phe	Phenylalanine	R	Arg	Arginine
G	Gly	Glycine	S	Ser	Serine
H	His	Histidine	T	Thr	Threonine
I	Ile	Isoleucine	V	Val	Valine
K	Lys	Lysine	W	Trp	Tryptophan
L	Leu	Leucine	Y	Tyr	Tyrosine



hydrophobic interaction (Figure 1.2).

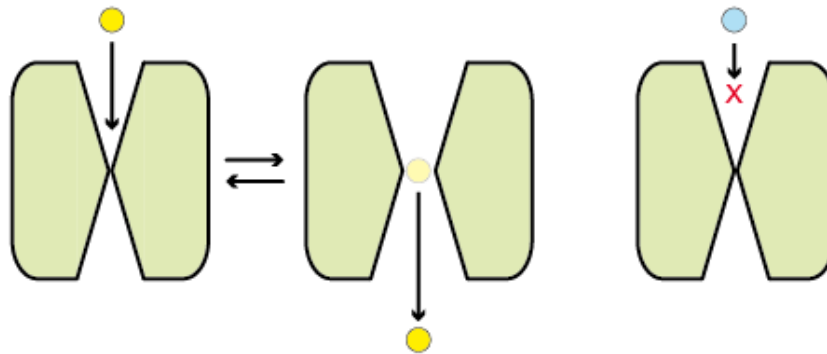


**Figure 1.2 Substrate recognition**

While transporters recognize specific substrates and translocate (left), non-substrates are neither recognized nor translocated (right).

Membrane transporters are categorized into two groups, according to their transport mechanisms. Those groups are uniporter and cotransporter. The transport by uniporter depends on only electrochemical gradients across the membrane, and thus its system is the passive transport. Cotransporters utilize the gradient of other chemical species to transport a certain substrate against the electrochemical gradient across the membrane. Moreover, cotransporters can be separated into different two categories. Transporting the substrate and the other chemical compound in the same or the opposite direction across membrane are defined as symporter and antiporter, respectively (Figure 1.3).

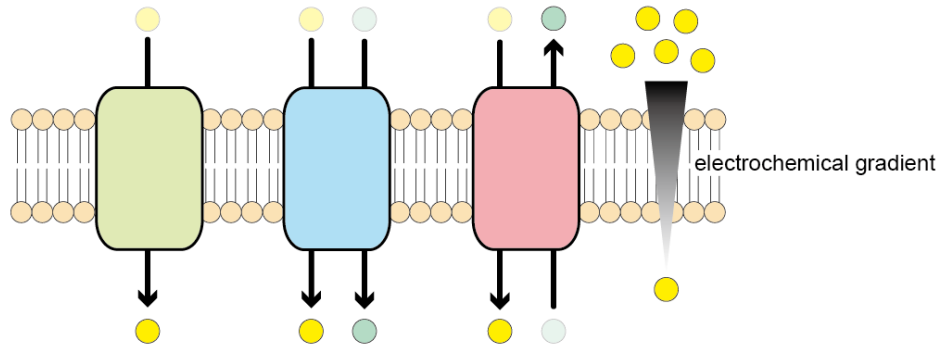


**Figure 1.3 Three types of transporters**

Light green, blue and red squares indicate uniporter, symporter and antiporter, respectively. When transporting substrates (yellow spheres) against chemical gradient, symporter and antiporter utilize other chemical species (green sphere).

All transporters show three conformations. In the occluded-state (OC), the pocket is isolated from both extracellular and intracellular solutions, and the substrates are not released in this state. Contrary in the outward-facing (OF) and inward-facing (IF) states, the pocket is faced toward extracellular and intracellular environments, respectively. Transporters show such conformation changes during the cycle, and this mechanism is widely known as “alternating access model”<sup>1,2</sup>. The its major model is defined as “Rocker-switch model”<sup>2</sup>. This model is carried out by symmetric movement of the transporter (Figure 1.4).

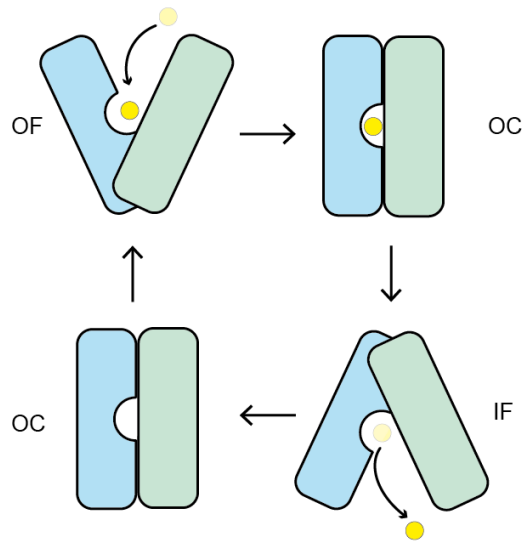


**Figure 1.4 Rocker-switch model**

Alternating access model shows three conformation states. Outward-facing (OF) and inward-facing (IF) states expose the pocket to solvent. Occluded-state (OC) seals the pocket. Rocker-switch model shows the symmetric movement of the transporter.

## **1-2 Iron ion homeostasis**

### **1-2-1 Iron ion as cofactor and toxin**

Many enzyme proteins need cofactors for their biochemical reactions. Especially, transient metal ions play key roles in various enzymatic reactions, and the importance of iron ion is widely conserved among all organisms. Extracellular iron ions are transported by transporters localized in plasma membrane, and many proteins, including electron transport chains<sup>3,4</sup> and DNA synthase<sup>5,6,7</sup>, utilize intracellular iron ions for the enzymatic reactions. However, excessive accumulation of iron ion generates reactive oxygen species (ROS) which directly damage biomolecules. Therefore, the concentration of intracellular iron ions is strictly regulated.

This regulation is carried out by many proteins. For instance, ferritin proteins isolate and store iron ions from the cytoplasmic solution to prevent the generation of ROS<sup>9</sup>. Moreover, transporters export from the intracellular solution to the extracellular environment to keep the low iron ion level<sup>10</sup>.

### **1-2-2 Plant iron ion homeostasis**

Ferritin is known as a main protein to regulate the intracellular concentration in eukaryotes, whereas plants adopt different mechanisms. For example, they secrete organic acids (e.g. citrate and mugineic acid) to extracellular ferrous or ferric ions, to stabilize their soluble forms<sup>11,12</sup>. These complexes are transported into cells and transported via vascular bundles for the long distance translocation<sup>13</sup>. Iron ions are also isolated in organelle vacuoles and stored until their use (Figure 1.5)<sup>14</sup>.

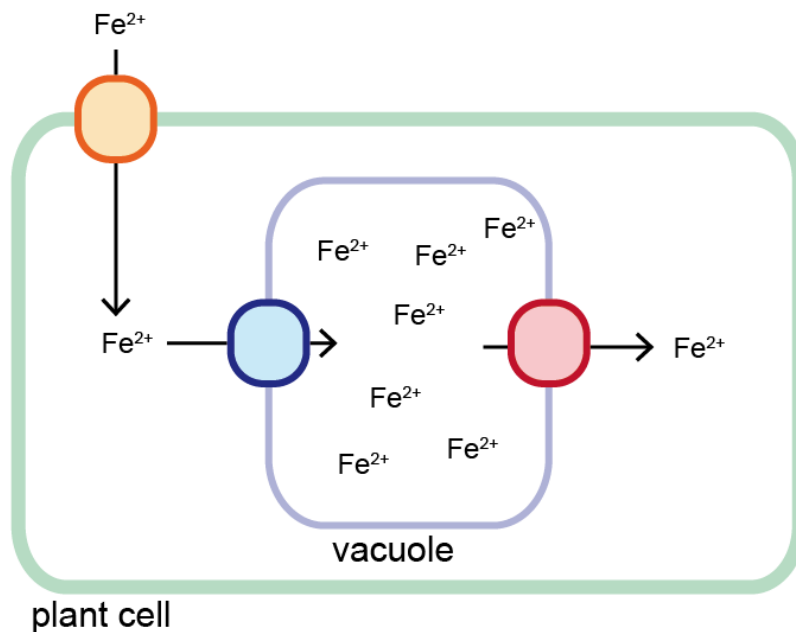


**Figure 1.5 Vacuole isolates and stores iron ions**

Cytoplasmic iron ions are transported by a vacuolar iron transporter (blue). Other transporter (red) pumps iron ion from vacuolar solution to supply iron ion. The function of vacuole is highly conserved among plant cells.

Vacuoles play a key role in several heavy metal ions homeostasis besides iron ions, and detailed mechanisms of vacuolar heavy metal transporters have been studied. However, the vacuolar transporter responsible for iron ion storage had been not identified until recently. In 2004, Vacuolar Iron Transporter 1 (VIT1) was identified as molecular entity of the iron transporter in vacuoles<sup>15</sup>. VIT1 is the homologue of the fungal vacuolar iron transporter Cross-Complements  $Ca^{2+}$  phenotype of the *csg1* (CCC1). VIT1 and CCC1 proteins are localized in vacuolar membranes and responsible for the iron ion accumulation in the vacuoles<sup>15</sup>.

## **1-3 Vacuolar Iron Transporter 1 (VIT1)**

### **1-3-1 Function of VIT1**

The gene of VIT1 was firstly identified in the genome of *Arabidopsis thaliana* and reported that VIT1 contributes to regulate the vacuolar iron concentration during the early development<sup>15</sup>. In addition to *Arabidopsis thaliana*, VIT1 modulates the iron translocation between sink and source in rice<sup>16</sup>, and blue coloration of flowers requires the VIT1 gene in tulip<sup>17</sup>.

In addition to basic plant physiological studies, some researchers focus on VIT1 gene for a gene modification of crops and a drug target for malaria. Some researches showed that crops overexpressing the VIT1 gene contain higher iron content than wild type<sup>18,19</sup>. As human assimilates iron ion from foods, a crop whose genome is modified by VIT1 may play a key role in the treatment for iron deficiency<sup>20</sup>. Recent study reported that the VIT1 homologue of malaria-causing parasite *Plasmodium falciparum* is closely related to the parasite cycle<sup>21</sup>. The *Plasmodium* strain which shows the resistance to preexisting drugs is a current serious problem<sup>22</sup>, and thus the development of a novel drug for malaria is being requested. As animal kingdom including human does not have the VIT1 homologue, the inhibitor for *Plasmodium* VIT1 may be safe and efficient drug<sup>23</sup>.

### **1-3-2 Structural feature of VIT1**

VIT1 family is highly conserved among all kingdoms, except for animal, and sequence alignment shows three types. Firstly, VIT1, which belongs to plant, fungi and *Plasmodium falciparum*, contains a five transmembrane (TM) segments and a

cytoplasmic loop located between second and third TM (Fig 1.6). Almost all VIT1

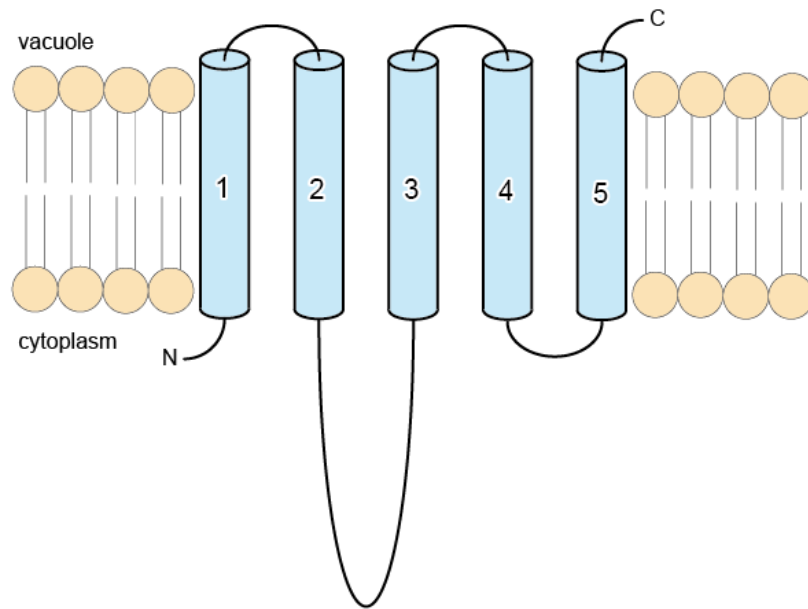


**Figure 1.6 Predicted topology of VIT1**

VIT1 contains predicted five TMs and the cytoplasmic loop located between second and third TM.

homologues show this topology. Secondly, plant Vacuolar iron transporter Like Transporters (VLTs) contain the transmembrane region, but they does not contain the cytoplasmic loop<sup>24</sup>. Finally, bacterial homologue Membrane-bound ferritin A (MbfA) is composed of the transmembrane region and N-terminal ferritin like domain, instead of the cytoplasmic loop<sup>25</sup>. Therefore, while the TM region is highly conserved among all homologues, cytoplasmic regions show diversity (Figure 1.7 and Alignment). Especially,

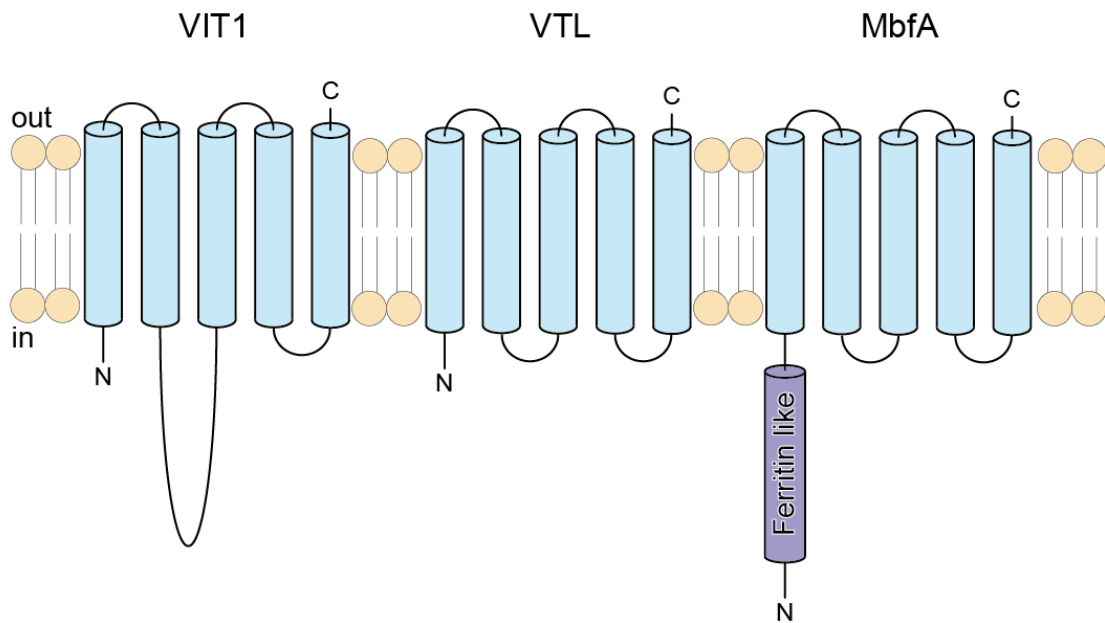


**Figure 1.7 Cytoplasmic diversity among VIT1 family**

Besides VIT1, VTL and MbfA belong to this family.

this region of VIT1 consists of several negative-charged residues. However, the role of cytoplasmic region has been unknown.

Although many structural studies have revealed atomic resolution structures about transporters, VIT1 does not share sequence similarities among those transporters, suggesting that the structure of VIT1 adopts a novel fold. Recent study reported that the *Plasmodium* VIT1 protein may function as  $\text{Fe}^{2+}/\text{H}^+$  antiporter<sup>26</sup>. This study speculated that *Plasmodium* VIT1 possesses several metal ion binding sites. However, the detailed molecular mechanism has been unclear yet. To understand the mechanism of VIT1, we have to determine the structure at high resolution.



## **Chapter 2 Structural analysis of VIT1**

### **2-1 Introduction**

As mentioned above, the detailed molecular mechanism of VIT1 has been unknown, due to lack of structural information. To answer this question, I aim at determining the atomic resolution structure, using X-ray crystallography.

### **2-2 Materials and methods**

#### **2-2-1 Plasmid construction of VIT1 for crystallography**

VIT1 homologues were inserted into the pYES2 [URA3] vector with the C-terminally-fused tobacco etch virus (TEV) protease cleavage site and His10-tag, by In-Fusion system. As all VIT1 homologues contain N-terminal flexible regions, these regions were truncated.

#### **2-2-2 Expression and purification of VIT1 protein**

The transformed budding yeast *Saccharomyces cerevisiae* BY4742 *pep4Δ* strain<sup>27</sup> was incubated in YNB medium containing CSM-Ura (complete supplement mixture that lacks uracil) and 2.0% raffinose at 30°C. Protein expression was induced with 2.0% D-(+)-galactose at 30°C for 21 hours. Harvested cells were broken in Buffer-A (50 mM Tris-HCl, pH 8.0, 150 mM NaCl and 10% glycerol) with 0.5 mM phenylmethylsulfonyl fluoride (PMSF), using a JN-20 microfluidizer (Jokou). The collected lysate was ultracentrifuged (125,000g, 1 hour, 4°C) to separate the membrane fraction. The membrane fraction was solubilized in Buffer-A containing 2.0% n-dodecyl-

$\beta$ -D-maltoside (DDM) and 0.4% cholesteryl hemisuccinate (CHS) at 4°C for 1 hour. The insoluble material was removed by ultracentrifugation (125,000g, 30 min, 4°C), and the soluble fraction was mixed with 10 mM imidazole and Ni-NTA Superflow resin (Qiagen) at 4°C for 1 hour. The resin was washed with Buffer-A containing 0.2% DDM, 0.04% CHS and 30–50 mM imidazole. The EgVIT<sub>123–249</sub> protein was eluted by the same buffer containing 300 mM imidazole. The sample was mixed with His-tagged TEV protease to cleave the His<sub>10</sub>-tag and was dialyzed to remove the imidazole, using Buffer-B (50 mM Tris-HCl, pH 8.0, 150 mM NaCl, 10% glycerol, 0.05% DDM and 0.01% CHS). The cleaved tag and TEV protease were removed by the Ni-NTA resin, and the flow-through sample was concentrated for subsequent gel filtration chromatography (Superdex 200 Increase 10/300 GL, GE Healthcare) in SEC-A buffer (50 mM Tris-HCl, pH 8.0, 150 mM NaCl, 0.05% DDM and 0.01% CHS). The fraction containing the EgVIT<sub>123–249</sub> protein was pooled, concentrated to 15 mg/mL using an Amicon Ultra filter (MWCO 50 kDa) and frozen until crystallization.

### **2-2-3 Expression and purification of isolated MBD protein**

The region encoding MBD (EgVIT<sub>190–165</sub>) was inserted into the pE-SUMO vector, with the N-terminally-fused His<sub>6</sub>-tag, small ubiquitin-related modifier (SUMO) and tobacco etch virus (TEV) protease cleavage site. The transformed *Escherichia coli* Rosetta2 (DE3) strain was incubated at 37°C to an OD<sub>600</sub> of 0.4–0.6, and protein expression was induced with 0.2 mM isopropyl- $\beta$ -D-thiogalactopyranoside (IPTG) at 20°C for 21 hours. The harvested cells were disrupted in Buffer-A containing 0.5 mM PMSF, using a JN-20 microfluidizer. The soluble fraction was mixed with 10 mM imidazole and Ni-NTA Superflow resin at 4°C for 1 hour. The resin was washed with

Buffer-A containing 20 mM imidazole, and the EgVIT1<sub>90-165</sub> protein was eluted with Buffer-A containing 300 mM imidazole. The sample was mixed with the His-tagged TEV protease to cleave the His6-SUMO, and was dialyzed against Buffer-A to remove the imidazole. The cleaved His6-SUMO and TEV protease were removed by the Ni-NTA resin. The flow-through sample was concentrated for subsequent gel filtration chromatography (Superdex 75 10/300 GL, GE Healthcare) in SEC-B buffer (50 mM Tris-HCl, pH 8.0, 150 mM NaCl). The fraction containing the EgVIT1<sub>90-165</sub> protein was pooled and concentrated to 10 mg/mL, using an Amicon Ultra filter (MWCO 10 kDa).

#### **2-2-4 Crystallization and structural determination of VIT1 protein**

Prior to crystallization, the purified EgVIT1<sub>23-249</sub> protein was incubated with 1.0 mM ZnCl<sub>2</sub> on ice for 1 hour. After this incubation, the protein solution was mixed with monoolein in a 2:3 protein to lipid ratio (w/w), using the twin syringe method<sup>28</sup>. Aliquots (50–80 nL) of the LCP mixture were dispensed onto a 96 well sitting plate (Violamo) and overlaid with 700–1,000 nL precipitant solution using a Gryphon LCP crystallization robot (Art Robbins Instruments). The crystals were obtained at 20°C in reservoir solution containing 100 mM HEPES-NaOH, pH 7.0, 250-300 mM (NH<sub>4</sub>)<sub>2</sub>SO<sub>4</sub>, 200 mM NaF, 0.4 mM ZnCl<sub>2</sub> and 24–26% PEG500DME, and grown for one month. The crystals were directly harvested from the plate without any cryo-protectant and flash-cooled. For the preparation of the mercury-derivative crystals, cysteine was introduced at Gly242 (EgVIT1<sup>G242C</sup>), and the mutant protein was expressed and purified using the same protocol. The purified EgVIT1<sup>G242C</sup> protein was incubated with 1.0 mM CH<sub>3</sub>HgCl on ice for 30 minutes and subsequently with 1.0 mM ZnCl<sub>2</sub> for 30 minutes. The crystals of Hg-

derivatized EgVIT1<sup>G242C</sup> were obtained under similar conditions to those for the wild-type protein. For the cobalt-soaking experiments, the reservoir solution of the Zn<sup>2+</sup>-bound crystals was replaced with the same solution (100 mM HEPES-NaOH, pH 7.0, 250-300 mM (NH<sub>4</sub>)<sub>2</sub>SO<sub>4</sub>, 200 mM NaF, 0.4 mM ZnCl<sub>2</sub> and 24–26% PEG500DME) containing 30 mM Co<sup>2+</sup> (cobalt (II) chloride) for 10 minutes. The crystals were directly harvested from the plate without any cryo-protectant and flash-cooled. The diffraction datasets were measured at the high-energy remote wavelength (1.280 Å).

Diffraction datasets were collected at the beamline BL32XU in SPring-8, using an EIGER X 9M detector at wavelengths of 1.2800 Å (Co<sup>2+</sup>-soaked) and 1.0000 Å (others). For EgVIT1<sub>23–249</sub>, 24 datasets (20-90°/crystal) were collected automatically using the ZOO system<sup>29</sup> with the helical scan method, and processed using the program XDS<sup>30</sup> with the data processing pipeline KAMO<sup>31</sup>. Hierarchical clustering was performed using BLEND<sup>32</sup>, and finally 5 datasets were merged after the outlier rejections implemented in KAMO. For EgVIT1<sup>G242C</sup>, several helical datasets were collected and processed manually using XDS and merged using XSCALE. From Co<sup>2+</sup> soaked crystals, 61 small-wedge (10°/crystal) and two helical (120°/crystal) datasets were collected, and processed and merged using KAMO pipeline with XDS. For the structural determination, the Hg site of the Hg-derivative EgVIT1<sup>G242C</sup> crystal was determined by the program SHELXD<sup>33</sup>, and the phases were determined using the program SHARP<sup>34</sup> with SIR method. The initial model was built on the map by Autobuild in PHENIX<sup>35</sup>, and further built manually and refined to the dataset of the native crystals by using COOT<sup>36</sup> and PHENIX, respectively. The Zn<sup>2+</sup> sites were aligned to the peaks in the anomalous difference maps, and restraints for the Zn<sup>2+</sup>-coordinating residues were applied in the final round of the refinement, using the high resolution structure of the isolated MBD

(EgVIT1<sub>90-165</sub>) as the reference model. The anomalous difference Fourier map for Co<sup>2+</sup>-soaked EgVIT1<sub>23-249</sub> was calculated by SHELXC<sup>37</sup> and ANODE<sup>38</sup>, using unmerged intensity data.

### **2-2-5 Crystallization and structural determination of isolated MBD**

For crystallization of the isolated MBD, the purified protein was also incubated with 1.0 mM ZnCl<sub>2</sub> on ice for 1 hour. Afterwards, 1.0 μL of the EgVIT1<sub>90-165</sub> protein solution was mixed with the same volume of the reservoir solution, containing 100 mM HEPES-NaOH, pH 7.0, 1.0-3.0 mM ZnCl<sub>2</sub> and 21-23% PEG600, and the crystals were grown for two weeks. For the metal-soaking experiments, the reservoir solution of the Zn<sup>2+</sup>-bound crystals was replaced with the same solution (100 mM HEPES-NaOH, pH 7.0, and 20% PEG600) containing 30 mM Ni<sup>2+</sup> (nickel (II) chloride), 30 mM Co<sup>2+</sup> (cobalt (II) chloride) or 20 mM Fe<sup>2+</sup> (1:1 molar ratio of ammonium iron (II) sulfate and ascorbic acid) for 10–20 minutes. The crystals were flash-cooled, using the reservoir solution supplemented with 20% glycerol as a cryoprotectant.

Diffraction experiments were performed at the beamline PXI X06SA in the Swiss Light Source and BL32XU or BL41XU in SPring-8. The diffraction datasets were measured at the peak and low-energy remote wavelengths of the respective X-ray absorption edges, namely 1.282 Å and 1.300 Å for the non-soaked (Zn<sup>2+</sup>-bound), 1.485 Å and 1.522 Å for the Ni<sup>2+</sup>-soaked, 1.605 Å and 1.648 Å for the Co<sup>2+</sup>-soaked, and 1.740 Å and 1.792 Å for the Fe<sup>2+</sup>-soaked crystals, respectively. The structure of EgVIT1<sub>90-165</sub> was determined by the zinc single-wavelength anomalous diffraction (Zn-SAD) method, using the dataset measured at 1.282 Å. The initial map and model were obtained by

Autosol in PHENIX<sup>35</sup>. The model was subsequently built manually and refined by COOT<sup>36</sup> and Refmac5<sup>39</sup>, respectively. As the analysis with the program Xtrriage<sup>35</sup> indicated twinning of the Ni<sup>2+</sup>-, Co<sup>2+</sup>-, and Fe<sup>2+</sup>-soaked crystals, intensity-based twin refinement was applied during the refinement process. The anomalous difference Fourier maps were calculated by using PHENIX. The figures depicting the molecular structures were prepared using CueMol (<http://www.cuemol.org/>).

## 2-3 Result

### 2-3-1 Purification and crystallization of *Eucalyptus grandis* VIT1

PSIPRED, which predicts the secondary structure and the disorder region of proteins, suggests that N-terminus of VIT1, including fungal homologue CCC1, show the disorder region (Figure 2.1), suggesting that this region prevents proteins from the

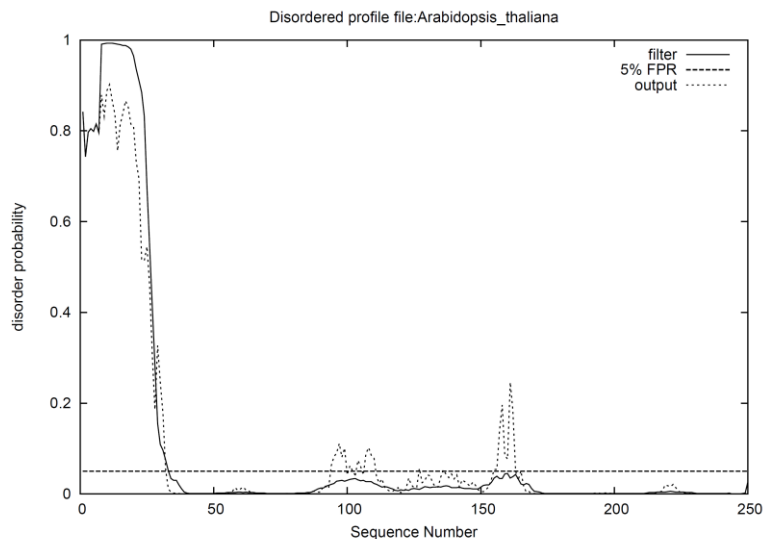


**Figure 2.1 Disorder prediction**

PSIPRED server (<http://bioinf.cs.ucl.ac.uk/psipred/>) suggests the N-terminal disorder region of VIT1.

crystallization. Therefore, I designed constructions, with N-terminal region deleted. Next, I inserted these genes into the budding yeast pYES vector, with C-termini fused both the TEV-protease recognition site and His<sub>10</sub> tag, and transformed into budding yeast BY4742 strain. Each homologue was expressed and solubilized, and I assessed both the expression

level and homogeneity. Judging from the size exclusion chromatography, a VIT1 gene from rose gum *Eucalyptus grandis* (EgVIT1) showed the highest expression and homogeneity levels than those of other homologues (Figure 2.2). In addition, purified EgVIT1 proteins also showed high thermostability when they are heated for 10 minutes (Figure 2.2). Therefore, I regarded EgVIT1 as a candidate for the structural trial. To

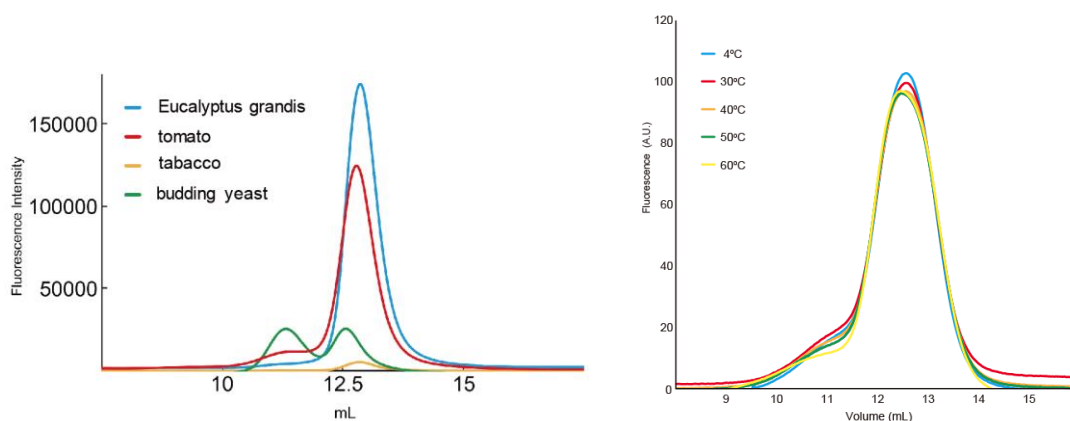


**Figure 2.2 Screening and thermostability of EgVIT1**

The expression level of EgVIT1 is higher than that of other homologues (left). Moreover, the purified EgVIT1 protein show high thermostability (right).

determine the structure, I performed crystallization trials of the purified EgVIT1<sub>23-249</sub> protein by the lipidic cubic phase (LCP) method, and proteins were successfully crystallized in the presence of zinc ions (Figure 2.3).

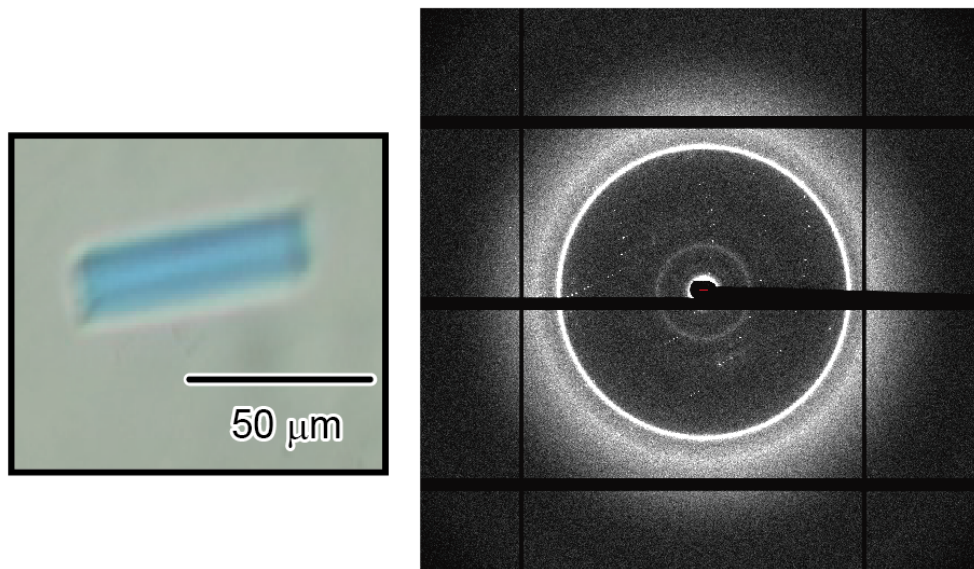


**Figure 2.3 Crystal of EgVIT<sub>123-249</sub> and X-ray diffraction pattern**

### 2-3-2 Structural determination of EgVIT1

As the cysteine residue strongly binds to mercury atom, structural researchers often try to soak it to crystals or prepare co-crystals to determine the experimental phase. However, EgVIT1 does not contain the cysteine residue. Sequence alignment indicates that Gly242 residue, which is located in fifth transmembrane helix, of EgVIT1 corresponds with Cys243 residue of AtVIT1 (Figure 2.4). I designed EgVIT<sub>123-249</sub><sup>G242C</sup>

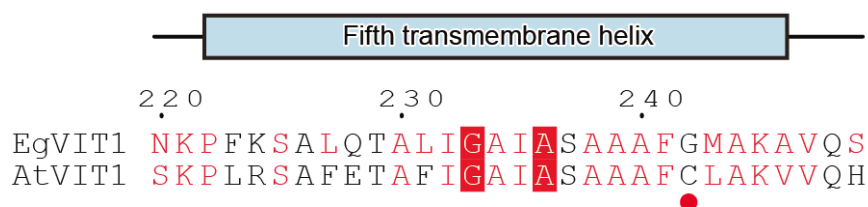


**Figure 2.4 Alignment between EgVIT1 and AtVIT1**

Sequence alignment shows Gly242 corresponds with Cys243 of AtVIT1 (red circle).

and purified it. Before the crystallization, I added methyl mercury chloride ( $\text{CH}_3\text{HgCl}$ ) to the purified protein and crystallized it by LCP method. Crystals were obtained in the presence of zinc ions as well as native crystals (Figure 2.5).

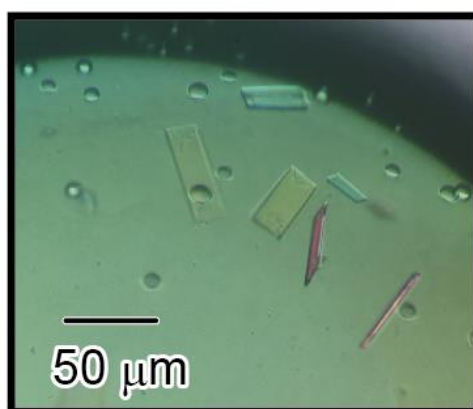


**Figure 2.5 Crystal of EgVIT<sub>123-249</sub> with Hg**

The phase was experimentally determined by the single isomorphous replacement (SIR) method, using mercury-derivatized crystals. All of the transmembrane helices (Glu32-Ser90 and Lys158-Ser249) were visualized and modeled in the clear electron density (Figure 2.6a, b). However, the electron density of the cytoplasmic region (Glu91-Glu157) was unclear, and thus this insufficient density prevented the model building (Figure 2.6a, c). It was probably due to the poor crystal packing in this region (Figure 2.7).

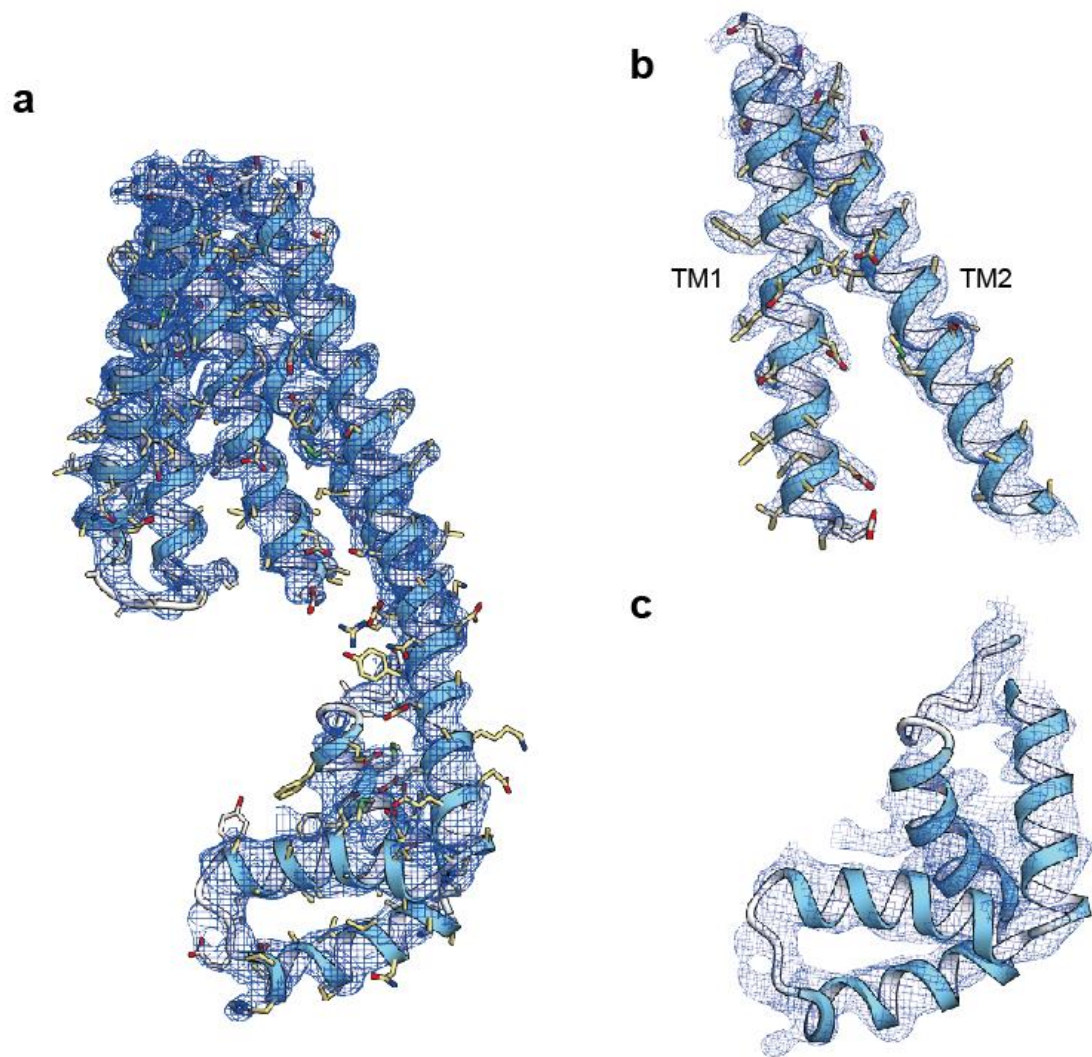


**Figure 2.6 Electron density of transmembrane and cytoplasmic regions**

(a) The electron density of overall structure ( $2Fo-Fc$  map contoured at  $1.0 \sigma$ ). (b) The electron density of the transmembrane helices. (c) The electron density of the cytoplasmic region.

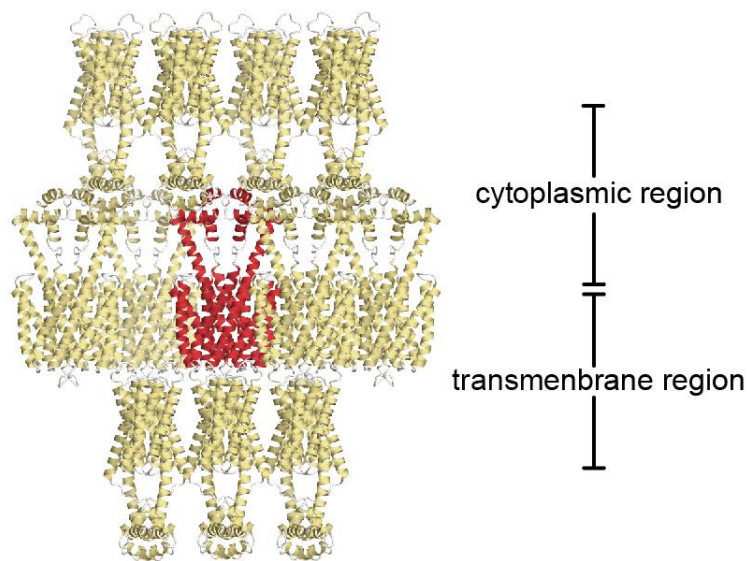


**Figure 2.7 Crystal packing of EgVIT1<sub>23-249</sub>**

Crystal packing of EgVIT1, viewed from the membrane plane. Red color shows the dimeric VIT1.

To enhance the model building of the cytoplasmic region, I expressed and purified the isolated cytoplasmic domain (EgVIT1<sub>90-165</sub>), which shows the unclear electron density in the structure of EgVIT1<sub>23-249</sub>, and crystalized it by the vapor diffusion method. Crystals were obtained in the presence of zinc ions, and I determined its structure at 2.25 Å resolution by the zinc single-wavelength anomalous diffraction (Zn-SAD) method (Figure 2.8 and Table 1). The clear electron density of the isolated cytoplasmic

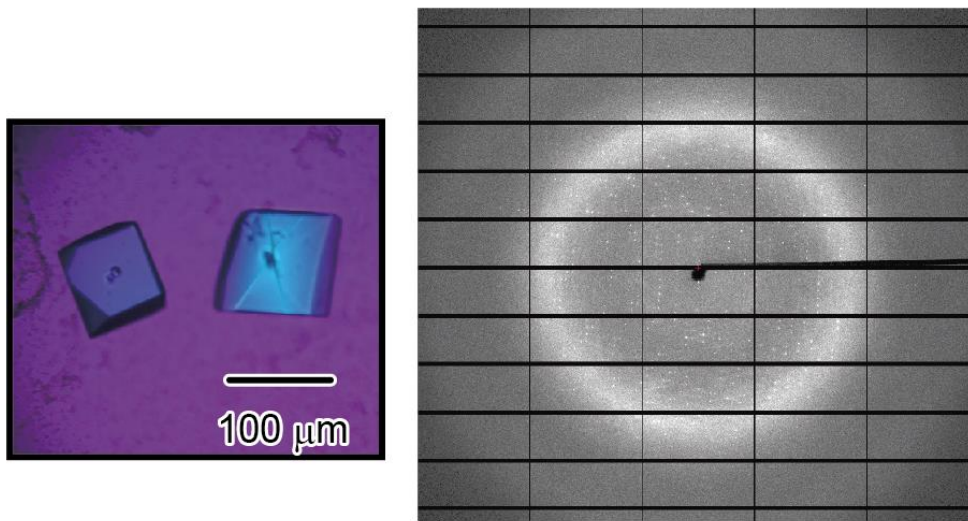


**Figure 2.8** Crystal of isolated cytoplasmic region and X-ray diffraction pattern

domain enabled me to construct a reliable model of the cytoplasmic domain (Figure 2.9), and using this structure as a reference, the full-length EgVIT<sub>123-249</sub> structure was determined at 2.7 Å (Table 2).

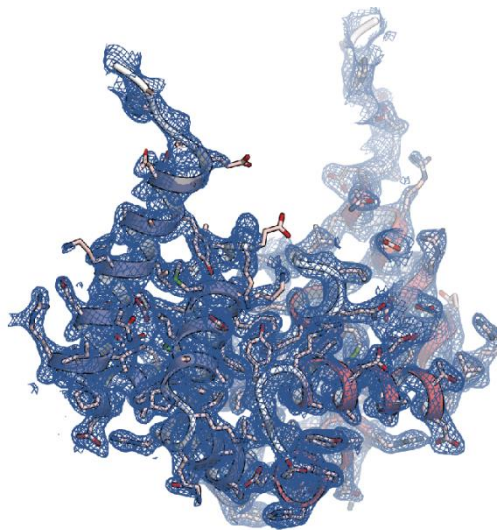


**Figure 2.9** Electron density of isolated cytoplasmic region

The electron density of isolated cytoplasmic region ( $2Fo-Fc$  map contoured at  $1.0 \sigma$ ).

### 2-3-3 Overall structure of EgVIT1

EgVIT1 forms a dimer. Each protomer is composed of the TransMembrane Domain (TMD) and the cytoplasmic Metal Binding Domain (MBD) (Figure 2.10). In

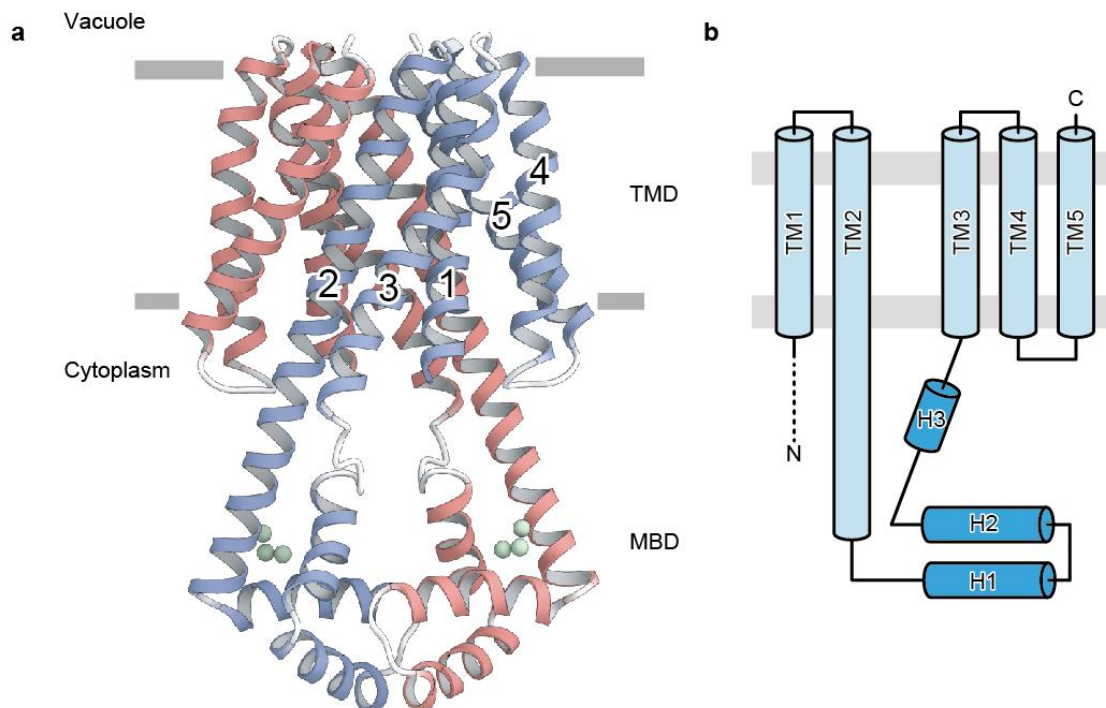


**Figure 2.10 Overall structure of EgVIT1**

(a) Overall structure of EgVIT1, as viewed from the membrane plane. Each number indicates TM1-TM5 helices. Zinc ions bound to the MBD shows green spheres. (b) Topology of EgVIT1.

agreement with the predicted topology about VIT1 family, each protomer consists of five transmembrane (TM) helices, with the N- and C-termini located in the cytoplasmic and the vacuolar lumen side, respectively. TM1 is located in the center of each protomer, and TM2–5 are arranged around TM1 in a clockwise order, as viewed from the cytosolic side

(Figure 2.11). The long TM2 helix protrudes from the lipid membrane by about 40 Å

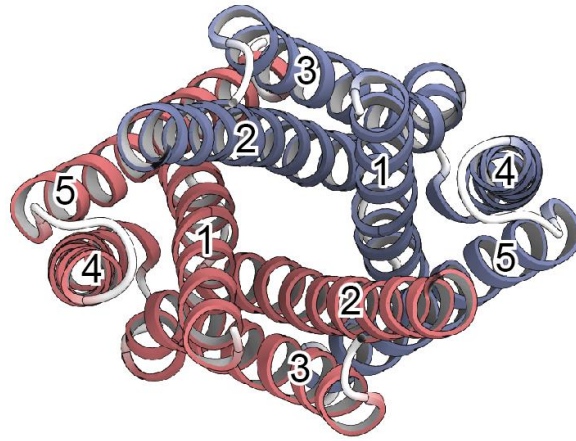


**Figure 2.11 Clockwise order**

The arrangement of the TM segments, viewed from the cytoplasm.

and is perpendicularly bent at its end, where it connects to the three cytoplasmic helices (H1–H3). H1 and H2 run parallel to the lipid membrane, and H3 head towards the membrane region and connects to TM3 via a short loop. The cytoplasmic region of TM2 and two helices, H1 and H3, are composed of the MBD, which harbors the binding sites for the zinc ions. The dimeric interaction is mediated by both TMD and MBD. In the TMD, TM1, TM2 and TM5 form a broad hydrophobic interface, while in the MBD, the bulky residues of the H2 helix, such as Phe148 and Phe152 (Figure 2.12), are oriented

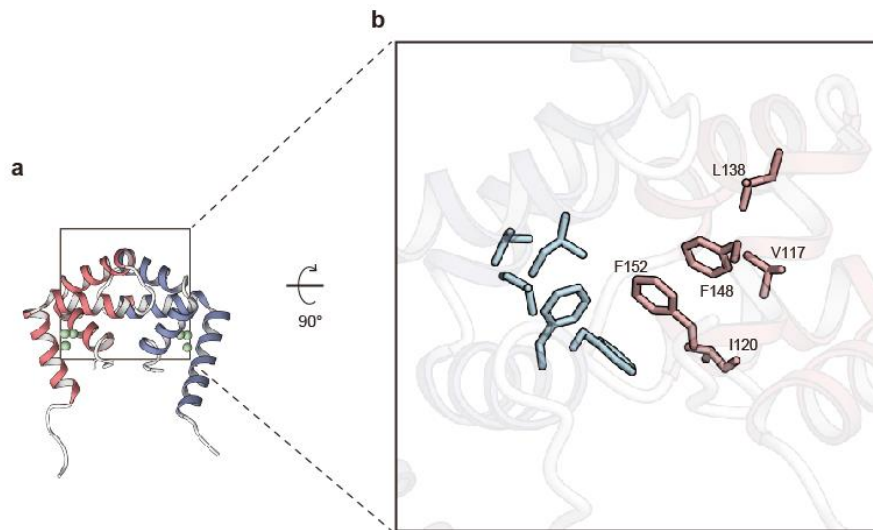


**Figure 2.12 Overview of the cytoplasmic region and hydrophobic interaction**

(a) The dimeric structure of the isolated cytoplasmic region. (b) Hydrophobic residues between the MBD dimer. Hydrophobic interactions occur between Val117 and Ile120 on H1, and Leu138 on H2 and Phe148 and Phe152 on H3.

toward the other protomer, contributing to the dimeric interactions. This protein fold of EgVIT1 is different from those of any known transporter structures ever reported, and represents a novel fold that is likely to be conserved among the VIT1 family members.



## **Chapter 3    Transport mechanism of VIT1**

### **3-1 Introduction**

I determined the structure of EgVIT1<sub>23-249</sub> and isolated cytoplasmic metal binding domain. As EgVIT1 adopts the novel fold, it is essential to investigate the molecular mechanisms, including the recognition of metal ion at TMD, the transport dynamics and the function of MBD. To reveal them, I and coworkers tried to design mutants based on structural information and analyze them *in vivo* and *in vitro*.

### **3-2 Materials and methods**

#### **3-2-1 Spot analyses (Fe<sup>2+</sup> sensitivity spot assay)**

The *S. cerevisiae* S21-I08 strain (BY4741<sup>27</sup> *ccc1::kanMZ*) was transformed with pYES2, pYES2-VIT1(wt) containing a C-terminal His10-tag, and its derivatives, and transformant colonies were obtained on SC-Ura plates. Each transformant was cultured in SC-Ura liquid medium at 30°C overnight. The next day, the liquid samples were diluted 1:10 with the same medium and grown until the OD<sub>600</sub> reached 1.0. The samples were then 10-fold serially diluted and spotted onto induction plates (SC-Ura medium containing 2% galactose) with/without 7.5 mM FeSO<sub>4</sub>. The plates were incubated at 32°C for three days, as indicated in the figure legends.

### **3-2-2 Preparation of proteolipomes**

The chloroform-solubilized lipid solution, containing a 3:1 weight ratio of 1-palmitoyl-2-oleoyl-*sn*-glycero-3-phosphoethanolamine (Avanti):1-palmitoyl-2-oleoyl-*sn*-glycero-3-phosphoglycerol (Avanti), with 12% egg phosphatidylcholine (Avanti) added, was dried and solubilized in a solution containing 50 mM HEPES-NaOH, pH7.0 or MES-NaOH, pH6.0, 150 mM NaCl and 1.0% n-decyl- $\beta$ -D-maltoside (DM). The purified protein was added to the solubilized lipid, at a 70:1 lipid to protein ratio (wt/wt). After a short incubation, Bio-Beads SM-2 (Bio-Rad) were added to remove the detergents in the mixture at 4°C overnight, and after the Bio-Beads were replaced with fresh ones, the mixture was incubated for an extra 3 hours at 25°C. The reconstituted proteoliposomal solutions were collected and stored at -80°C. To confirm the reconstitution, proteoliposomal solutions were ultracentrifuged (125,000g, 15 minutes, 4°C) to separate proteoliposomes. The proteoliposomal fractions were solubilized in the buffer (50 mM Tris-HCl, pH8.0, 150 mM NaCl, 1.0% DDM and 0.2% CHS) at 4°C for 1 hour. The insoluble material was removed by ultracentrifugation (125,000g, 15 min, 4°C) and solutions were collected for subsequent gel filtration chromatography (Superdex 200 Increase 10/300 GL, GE Healthcare) in SEC-A buffer.

### **3-2-3 Liposomal assay**

The proteoliposomes were mixed with same volume of buffer, containing 50 mM HEPES-NaOH, pH 7.0 or MES-NaOH, pH6.0, 150 mM NaCl, and 500  $\mu$ M calcein, subjected to three cycles of freezing-thawing, and then sonicated for 30 seconds using a Bioruptor (CosmoBio). The extraliposomal calcein was removed by chromatography on Sephadex G-50 fine resin (GE Healthcare). The liposome solution (20  $\mu$ L) was suspended

in 480  $\mu\text{L}$  of extraliposomal solution, containing 50 mM buffer (MES-NaOH, pH 6.0, HEPES-NaOH, pH 7.0, or HEPES-NaOH, pH 8.0) and 150 mM NaCl, and then the calcein fluorescence ( $\lambda_{\text{ex}} = 494 \text{ nm}$  and  $\lambda_{\text{em}} = 516 \text{ nm}$ ) was monitored at 30°C, using an F7000 fluorescence spectrophotometer (Hitachi). In the  $\text{Zn}^{2+}$ -competition assay, 10  $\mu\text{M}$   $\text{ZnCl}_2$  was added in the extraliposomal solution.  $\text{Fe}^{2+}$  (10:1 molar ratio of ammonium iron (II) sulfate and sodium dithionite diluted in the inner solution) or  $\text{Co}^{2+}$  was added (final concentration 10  $\mu\text{M}$ ) after 300 seconds, and the  $\text{Fe}^{2+}$ - and  $\text{Co}^{2+}$ -dependent quenching was recorded for the next 300 seconds. In the measurements using carbonyl cyanide m-chlorophenyl hydrazone (CCCP), 50 mM MES-NaOH, pH 6.0, and 50 mM HEPES-NaOH, pH 8.0, were used for the intraliposomal and extraliposomal buffers, respectively. CCCP dissolved in ethanol (final concentration 10  $\mu\text{M}$ ) or same volume ethanol (control) were added after 30 seconds, and  $\text{Co}^{2+}$  was added after next 270 seconds.  $\text{Co}^{2+}$ -dependent quenching was recorded for the next 300 seconds. In the proton counter-transport assay, the proteoliposomes were prepared as described, but with the interliposomal solution containing 5 mM MES-NaOH pH, 6.0, 150 mM NaCl and 1.0 mM pyranine. The liposome solution (20  $\mu\text{L}$ ) was suspended in 480  $\mu\text{L}$  of extraliposomal solution, containing 5 mM HEPES-NaOH, pH 8.0, and 150 mM NaCl, and the substrate  $\text{Co}^{2+}$  was added (final concentration 10  $\mu\text{M}$ ) after 300 seconds. The pyranine fluorescence ( $\lambda_{\text{ex}} = 460 \text{ nm}$  and  $\lambda_{\text{em}} = 510 \text{ nm}$ ) was recorded for the next 300 seconds at 30°C and normalized to the intensity before the  $\text{Co}^{2+}$  addition. All measurements were repeated at least three times, and one representative trace for each mutant is shown.

### 3-3 Result

#### 3-3-1 EgVIT1 functions as H<sup>+</sup>-coupled antiporter

Although previous researches studied plant VIT1 homologues from *Arabidopsis thaliana*<sup>15</sup>, *Oryza sativa*<sup>16</sup> and *Tulipa gesneriana*<sup>17</sup>, the functional research about EgVIT1 has not been reported. Firstly, we confirmed the transport activity of EgVIT1, using a complementation assay in the budding yeast *Saccharomyces cerevisiae* (collaboration with Prof. Koichi Ito and Dr. Miki Wada). Cross-Complements Ca<sup>2+</sup> phenotype of the *csg1* (CCC1), which is encoded in the budding yeast genome, transports excessive cytoplasmic iron ion into vacuolar solution to maintain cytoplasmic iron level low<sup>40</sup>. Therefore, its deletion strain (*ccc1Δ*) shows the growth inhibition by the accumulation of cytoplasmic iron ion. Overexpression of EgVIT1<sub>23-249</sub> (the crystalized construction) successfully complemented this growth inhibition, indicating that the truncated EgVIT1<sub>23-249</sub> construct functions as the vacuolar iron transporter in yeast as well as AtVIT1<sup>15</sup> (Figure 3.1).

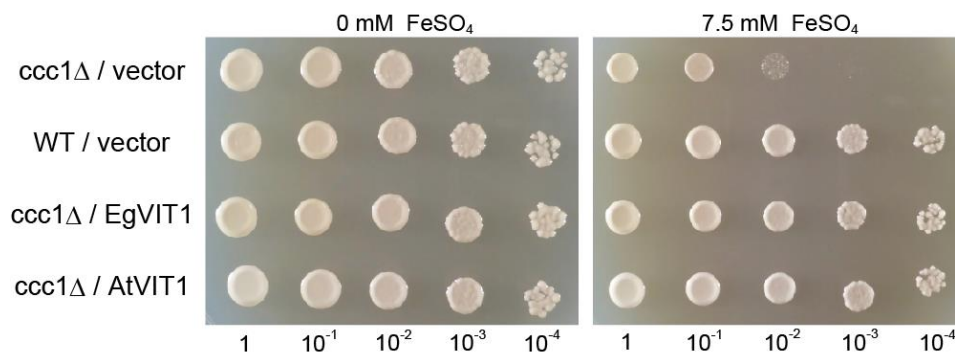


**Figure 3.1 Yeast spot assay**

Spot assay of the yeast *ccc1Δ* strain. *ccc1Δ* cells were transformed with each vector, inoculated under both conditions (0 or 7.5 mM iron(II) sulfate), and incubated at 32°C for 3 days.

Next, I measured the transport activity *in vitro*, using proteoliposome. The purified EgVIT1<sub>23-249</sub> protein is reconstituted into liposomes, and I measured its iron transport activity using calcein, a fluorescence indicator for divalent cations<sup>41,42</sup> (Figure 3.2). The addition of Fe<sup>2+</sup> to the extraliposomal solution induced a quenching of the

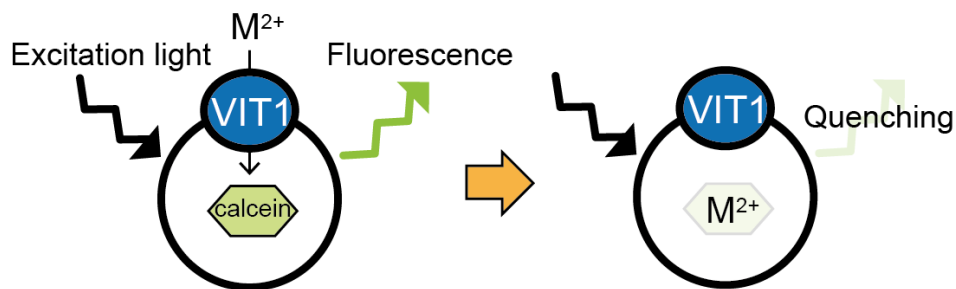


**Figure 3.2 Liposomal assay by divalent cation indicator calcein**

Principle of liposomal assay, using divalent cation ( $M^{2+}$ ) indicator calcein. Non- $M^{2+}$  bound calcein emits the fluorescence, whereas  $M^{2+}$ -binding induces quenching of the fluorescence of calcein.

calcein fluorescence, whereas this quenching was much smaller in the empty liposomes, indicating that EgVIT1 transports Fe<sup>2+</sup> into intraliposomal solution (Figure 3.3).

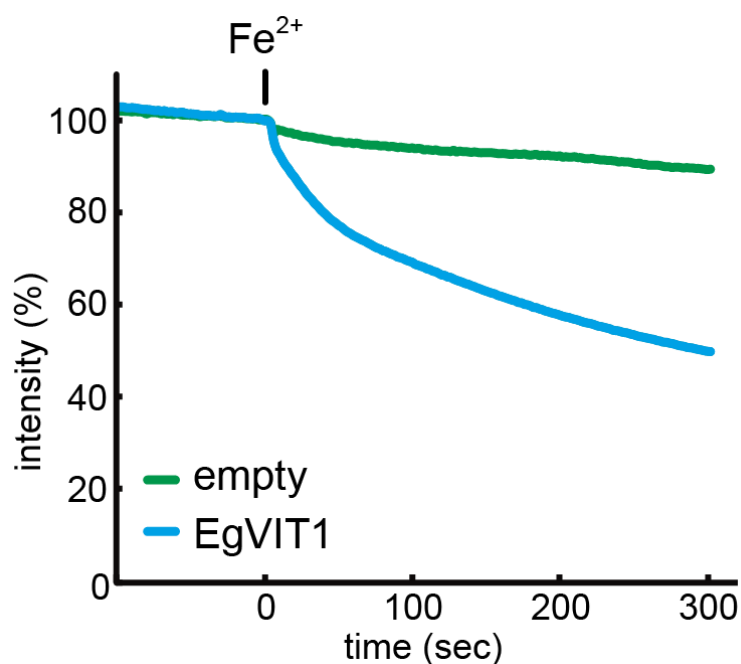


**Figure 3.3 EgVIT1 transports iron ion *in vitro***

EgVIT1<sub>23-249</sub>-mediated transport of ferrous ion with the intraliposomal and extraliposomal pH values of 7.0 and 8.0, respectively. The fluorescence intensity of the liposomes was measured for 300 seconds, using the divalent cation indicator calcein.

Similar quenching was induced by adding cobalt ions to the extraliposomal solution, and thus EgVIT1 transports not only iron ions but also cobalt ions. To investigate the driving force of EgVIT1, I focused on the H<sup>+</sup> gradient and measured the transport activity with extraliposomal solutions with different pH values, as previous study suggested the Fe<sup>2+</sup>/H<sup>+</sup> antiporter activity of *Plasmodium* VIT1<sup>26</sup>. As Fe<sup>2+</sup> are sensitive to the pH and are easily oxidized at an alkaline pH, I used cobalt ions, instead of ferrous ions, as the transport substrate. When the intraliposomal pH was kept at 7.0, an extraliposomal solution at pH 8.0 increased the cobalt-dependent quenching, whereas an extraliposomal solution at pH 6.0 significantly decreased this quenching (Figure 3.4a). This quenching was further enhanced by the intraliposomal low pH conditions (pH 6.0) (Figure 3.4b).

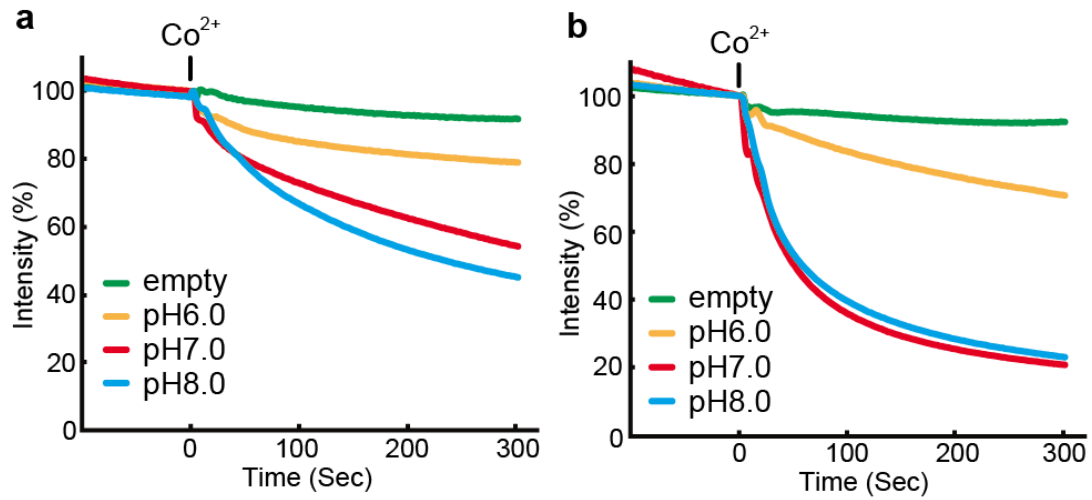


**Figure 3.4 pH has an influence on the transport activity of EgVIT1**

The  $\text{Co}^{2+}$  transport activity of EgVIT1, measured with different extraliposomal pH values for 300 seconds. Each measurement was performed with the intraliposomal solution pH of 7.0 (a) or 6.0 (b).

Furthermore, the proton ionophore Carbonyl Cyanide *m*-ChloroPhenylhydrazone (CCCP) significantly decreased the quenching (Figure 3.5), suggesting that the pH

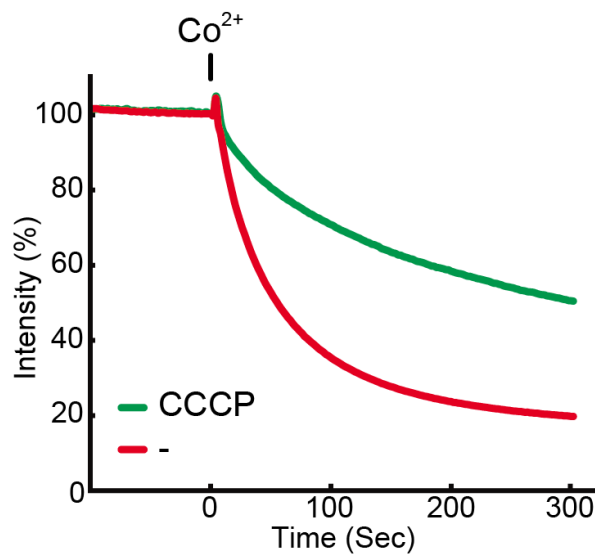


**Figure 3.5 CCCP decreases the transport activity of EgVIT1**

H<sup>+</sup>-specific ionophore carbonyl cyanide m-chlorophenyl hydrazone (CCCP) decreased the Co<sup>2+</sup>-transport activity of EgVIT1. The measurement was performed with the intra- and extraliposomal pH of 6.0 and 8.0, respectively.

gradient across the membrane has a significant influence on the metal ion transport by EgVIT1. I next examined the proton transport activity by EgVIT1, using H<sup>+</sup> indicator pyranine (Figure 3.6). When the pH indicator pyranine was loaded into the

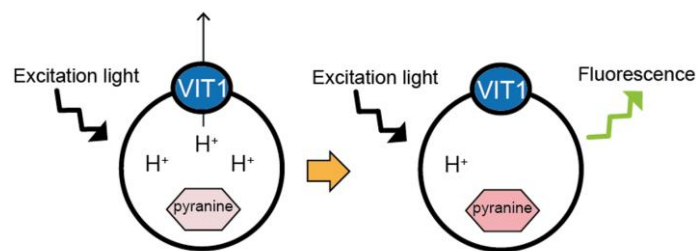


**Figure 3.6 Liposomal assay by proton indicator pyranine**

Principle of liposomal assay, using proton indicator pyranine. The fluorescence intensity of pyranine is increased by the reduced concentration of intraliposomal proton.

proteoliposomes<sup>43</sup>, the fluorescence intensity was increased by the addition of the metal ions, indicating the substrate-dependent proton transport from the intraliposomal solution, while the empty liposomes did not show such transport (Figure 3.7).

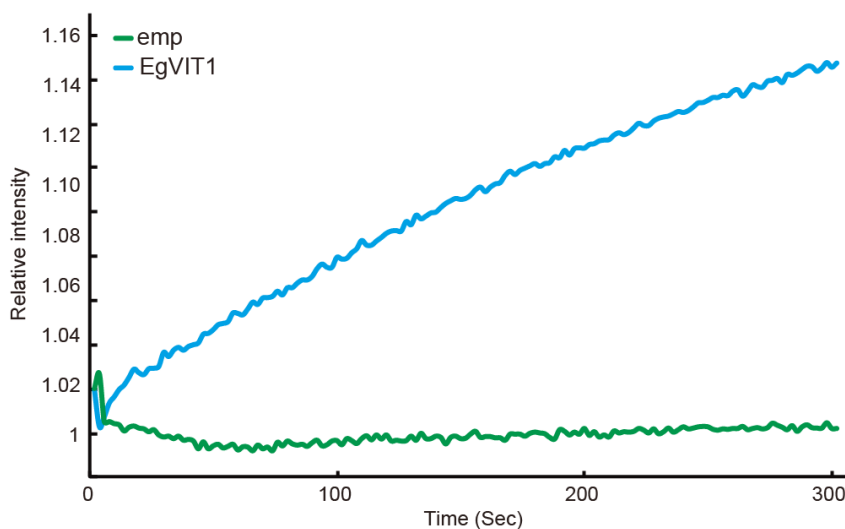


**Figure 3.7 EgVIT1 transports proton**

Measurement of the proton transport activity, using the pH indicator pyranine. The measurement was performed with intra- and extraliposomal pH values of 6.0 and 8.0, respectively.

Taken together, these results suggest that EgVIT1 is a H<sup>+</sup>-coupled metal ion antiporter.

### 3-3-2 Ion transport pathway at transmembrane domain

The two protomers form a large cavity at the dimer interface, which faces the cytoplasmic solution. This cavity extends to the middle of the membrane region, where four residues, Asp43 (TM1), Glu72 (TM2), Met80 (TM2) and Tyr175 (TM3) from each

protomer form a hydrophilic pocket (Figure 3.8). In particular, Asp43 and Met80, located

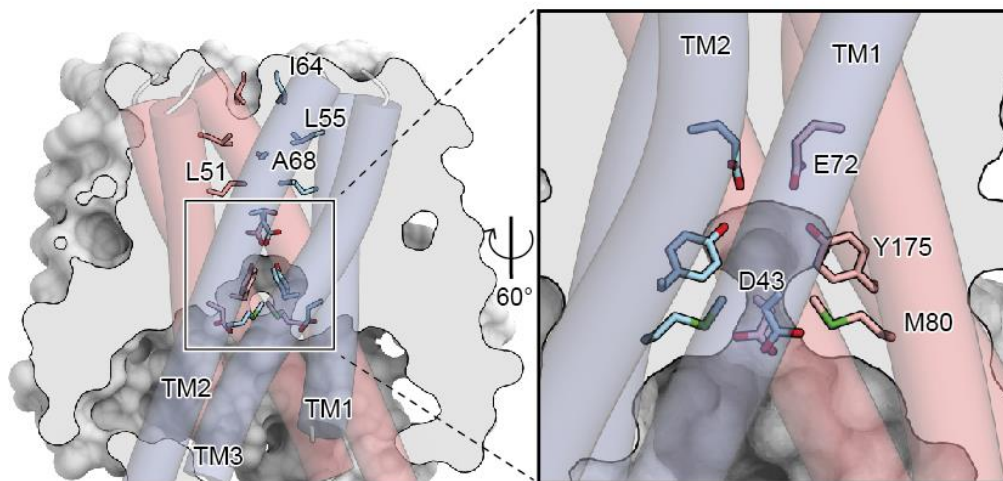


**Figure 3.8 Hydrophilic pocket at TMD**

Cut-away representation of TMD and close-up views of the hydrophilic pocket.

at the cytoplasmic entrance of this pocket, are completely conserved among the VIT1 family (Alignment). Therefore, I propose that the substrate metal ions are translocated along the central dimer axis of VIT1. Consistently, our study suggested that mutants of the above residues within the central translocation pathway failed to complement the growth inhibition of *ccc1Δ* in the yeast complementation assay (Figure 3.9a). Moreover, all mutants decrease the transport activity in the liposome assay (Figure 3.9b), indicating

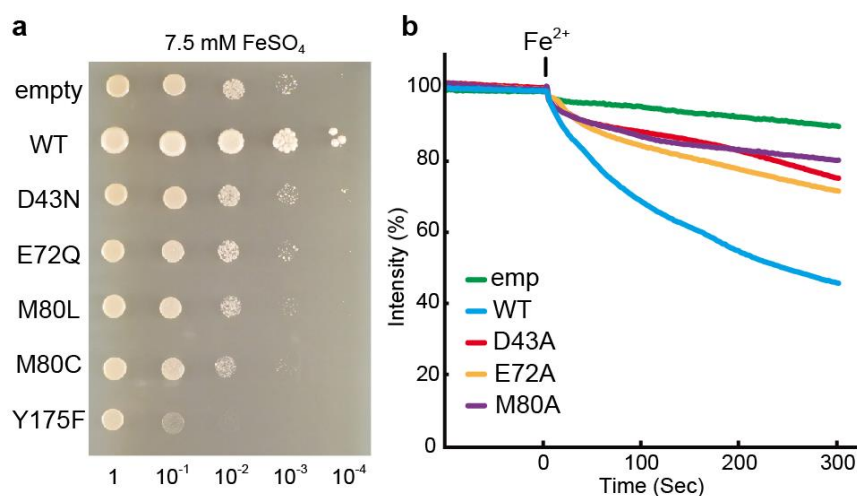


### Figure 3.9 Transport activity of mutants of the hydrophilic pocket

(a) Spot assay of mutants of pocket residues, performed under the same conditions as in Figure 3.1. (b) Liposomal assays for point mutants (Asp43Ala, Glu72Ala and Met80Ala). The Fe<sup>2+</sup>-dependent quenching was measured for 300 seconds. These measurements were performed with the intra- and extraliposomal solution pH at 7.0 and 8.0 respectively.

these residues contribute to the metal ion transport.

In the general transporter mechanism, a substrate binding pocket is alternately exposed to either side of the membrane, while preventing the leakage of the substrate or other solutes. In the current structure, the ion translocating pathway is sealed on the vacuolar lumen side for over 10 Å by hydrophobic residues, such as Leu51 and Leu55 on TM1 and Ile64 and Ala68 on TM3, and thus it is likely to represent the inward-facing state (Figure 3.8). To understand the detailed mechanism of the metal ion translocation and recognition, I soaked the Zn<sup>2+</sup>-bound EgVIT<sub>123-249</sub> crystals with the substrate Co<sup>2+</sup> and collected the dataset at the high energy remote wavelength of Co<sup>2+</sup>. The anomalous difference Fourier peak showed Co<sup>2+</sup> ion binding within the cytoplasmic hydrophilic pocket, coordinated by Asp43 and Met80 from each protomer (Figure 3.10). Taken

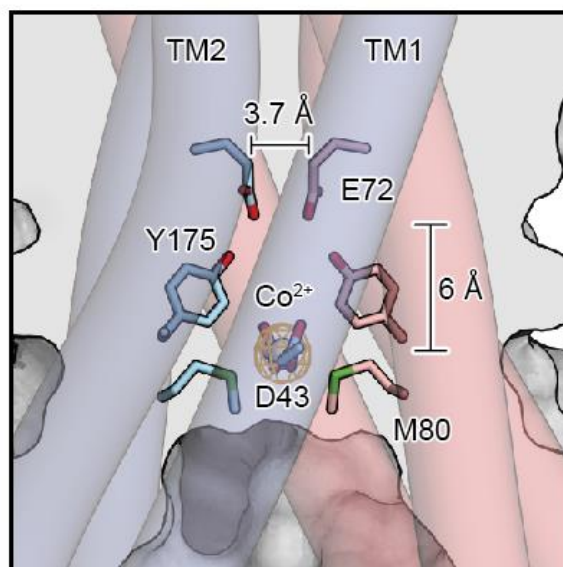


**Figure 3.10 Cobalt ion is coordinated by the hydrophilic pocket**

Close-up views of the hydrophilic pocket, with the anomalous difference density depicting the bound  $\text{Co}^{2+}$  ion (contoured at  $3.5 \sigma$ ), shown as an orange mesh. The distances between the cobalt ion and Glu72 (6 Å) and between the two Glu72 sidechains (3.7 Å) are indicated.

together, the hydrophilic pocket functions as the ion translocation pathway.

TM1 and TM2 contain several kink-inducing residues (Gly44 and Pro48 in TM1 and Gly69 and Gly76 in TM2), which are highly conserved among the VIT1 family (Alignment). I observed the  $\text{Co}^{2+}$ -induced kink movement of TM1 and TM2 caused by Gly44 and Gly76, respectively (Figure 3.11a). Mutations of Gly44 and Gly76, as well as Pro48 and Gly69, to alanine significantly decrease the metal ion transport activity in the liposome assay (Figure 3.11b), suggesting these residues are also important for the transport.

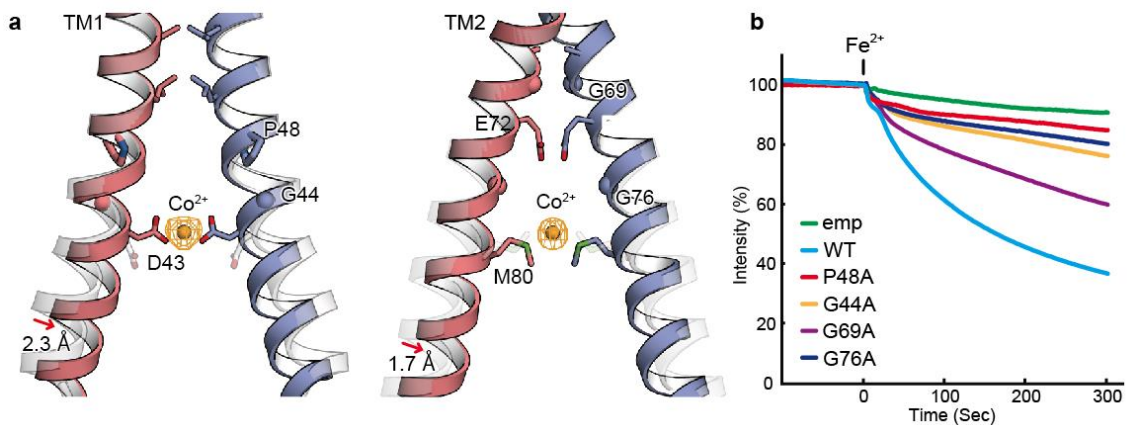


**Figure 3.11 Kink-induced residues**

(a) Inward motions of TM1 (left) and TM2 (right) induced by  $\text{Co}^{2+}$  soaking are shown. The  $\text{Co}^{2+}$ -soaked and non-soaked crystal structures are shown in opaque (cyan and pink) and transparent (grey) representations, respectively. Residues important for ion translocation are shown by sticks, with the glycine residues indicated by spheres. Red arrows indicate the inward motions of TM1 and TM2, with the distances indicated in angstroms. (b) Liposomal assays for the point mutants of the “kink-inducing” residues (Gly44Ala, Pro48Ala, Gly69Ala and Gly76Ala). These measurements were performed with the intra- and extraliposomal pH at 7.0 and 8.0, respectively.

The liposomal analysis indicated that EgVIT1 concurrently transports metal ion and proton. Consistently, the hydrophilic pocket consists of two acidic residues (Asp43 and Glu72) from each protomer. These mutants significantly decrease the proton transport activity (Figure 3.12).

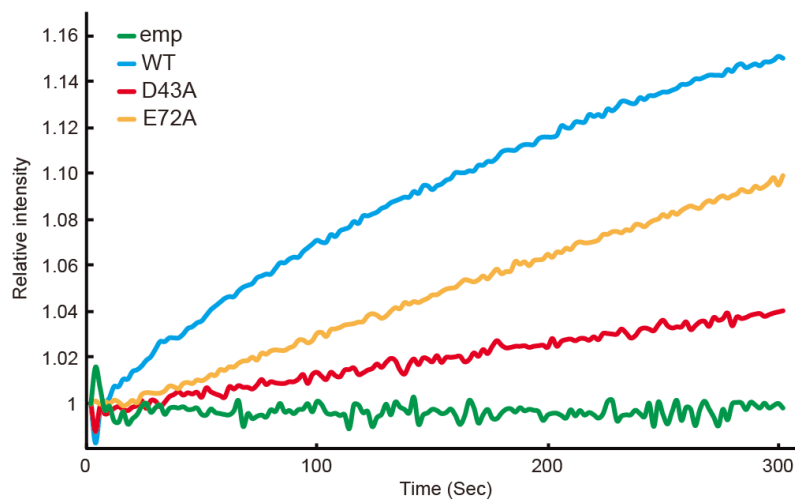


**Figure 3.12 Measuring H<sup>+</sup> transport**

Liposomal assay for mutants of acidic residues (Asp43 and Glu72) located in the hydrophilic pocket.

### 3-3-3 Function of cytoplasmic metal binding domain

Next, I investigated the role of MBD in the ion transport. The strong X-ray anomalous scattering signals clearly identified the zinc ion binding sites of the MBDs in both the EgVIT<sub>123-249</sub> and isolated MBD structures (Figure 3.13). In both structures,

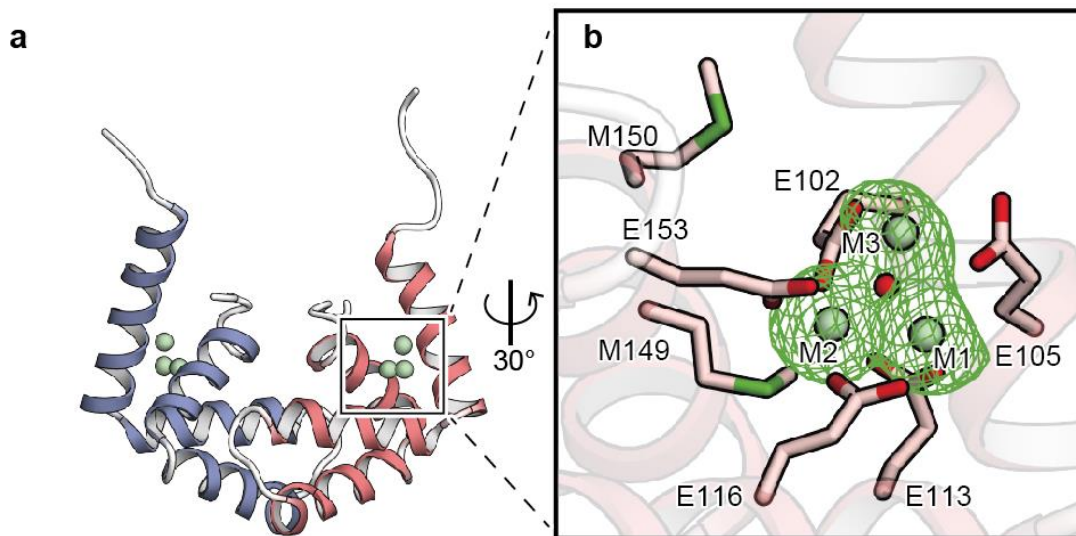


**Figure 3.13 Structure of MBD**

(a) Structure of the isolated MBD (EgVIT<sub>190-165</sub>). (b) Close-up view of the metal binding site depicting the anomalous difference density of the zinc ion (contoured at  $3.5 \sigma$ ), shown as a green mesh. The three zinc ions (M1–M3) are depicted as green spheres, and OH<sup>-</sup> or O<sup>2-</sup> is a red sphere.

three zinc ions are coordinated by five glutamate residues (Glu102, Glu105, Glu113, Glu116 and Glu153) and one methionine residue (Met149) (Figure 3.14). The high-

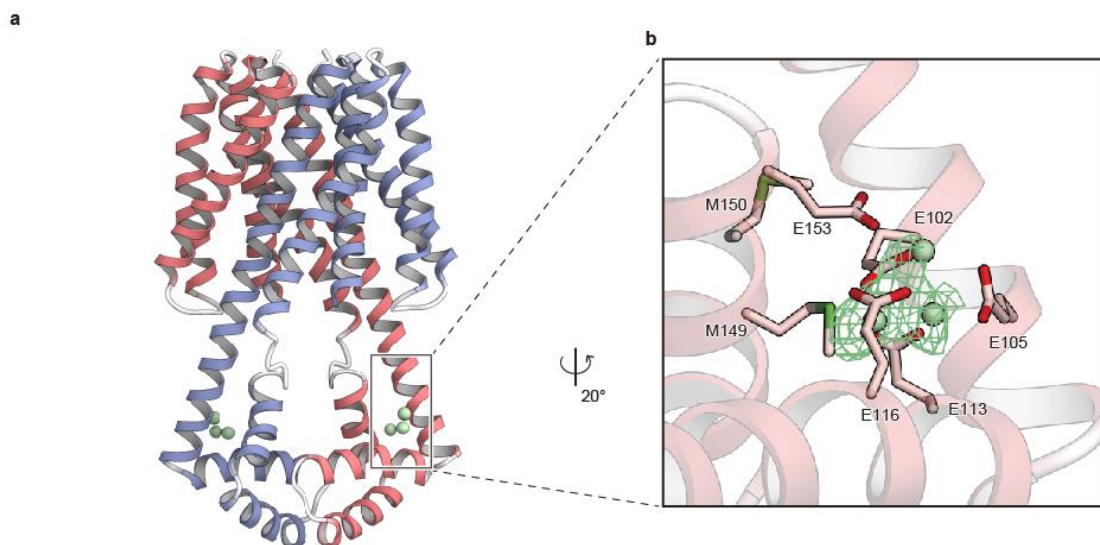


**Figure 3.14 Anomalous density of the zinc ion in EgVIT<sub>123-249</sub>**

(a) The anomalous signals of the EgVIT<sub>123-249</sub> structure. (b) Close-up view of the anomalous difference density of zinc ions (contoured at 3.5  $\sigma$ ), shown as a green mesh.

resolution of the isolated MBD revealed that three zinc ions are clustered within unusually proximal distances of about 2.5 Å (Figure 3.15), where a water molecule, probably in the

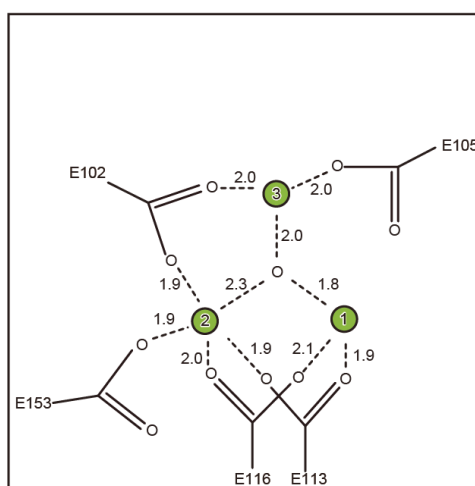


**Figure 3.15 Metal binding site at MBD**

Coordinating three zinc ions. Five glutamate are involved in metal ion coordination.

$\text{OH}^-$  or  $\text{O}^{2-}$  form, occupies the center of this triad cluster and forms semi-covalent bonds with these ions. To investigate the MBD further, the  $\text{Zn}^{2+}$ -bound MBD crystals were soaked in solutions of several transition metal ions and subjected to diffraction experiments, using slightly shorter wavelengths than the respective X-ray absorption edges. The anomalous difference Fourier map peaks showed that these metal ions differently replace and occupy one or two of the three zinc binding sites (M1 to M3) (Figure 3.16). Notably, all of these metal ions commonly occupy the M2 site, in which

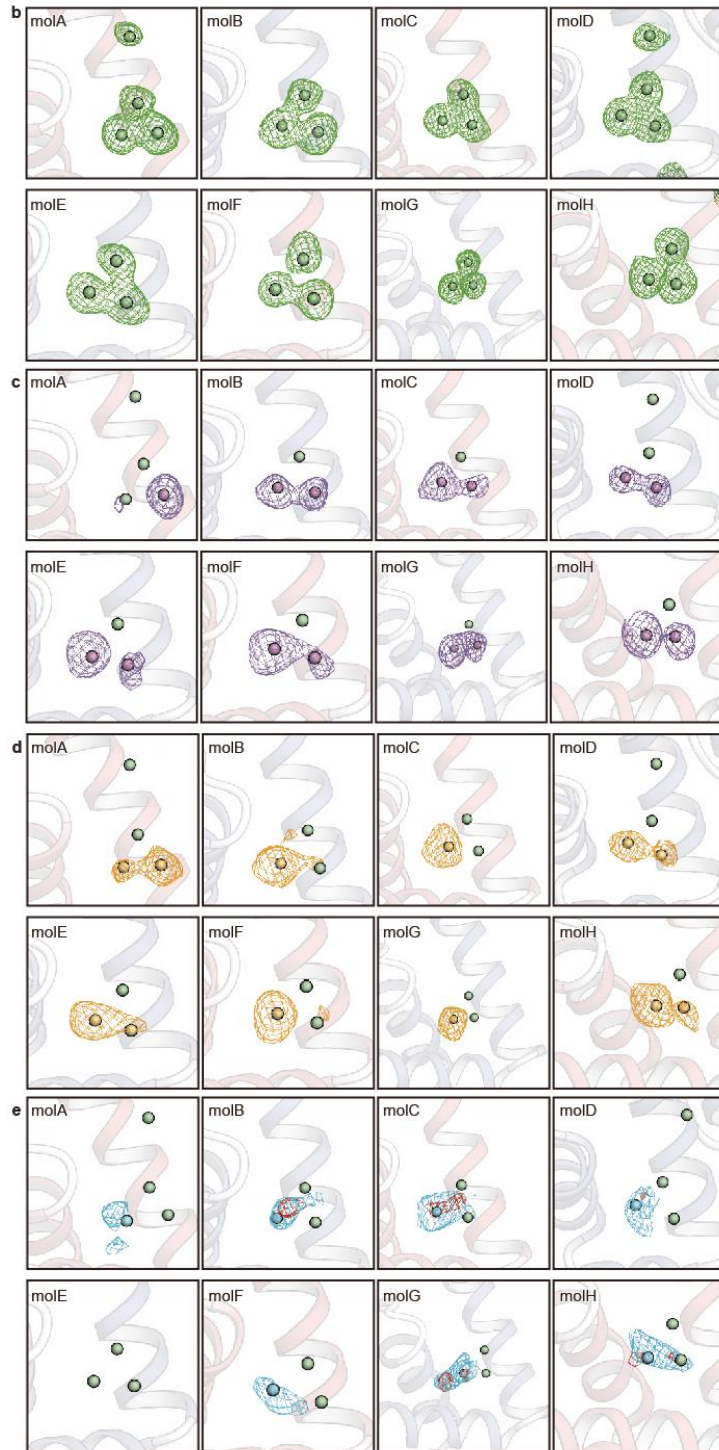
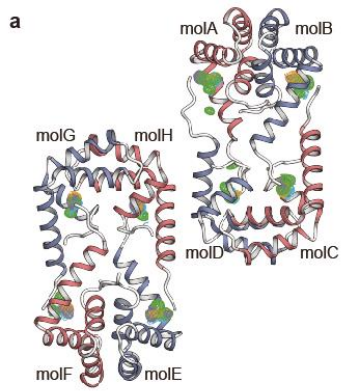


### Figure 3.16 Anomalous difference densities of metal ions bound to MBD

(a) Eight monomers (MolA–MolH) in the asymmetric unit of the isolated MBD crystal show slightly different occupancies for each metal ion. (b–e) Close-up views of the metal binding sites in each monomer. Anomalous difference densities (contoured at  $3.5 \sigma$ ) of zinc (b), nickel (c), cobalt (d) and iron (e) are shown as green, purple, orange, and cyan meshes, respectively. For the  $\text{Fe}^{2+}$ -soaked crystals, we also observed weak anomalous difference densities even in the dataset collected at the low-energy remote wavelength (contoured at  $3.5 \sigma$ , red meshes), which might be due to the slight shift of the absorption energy by the iron oxidization.

the sulfur-containing methionine residue (Met149) participates in the ion binding, indicating the importance of methionine residue for the transition metal ion binding (Figure 3.17). Overall, these results suggested that the MBD captures various transition

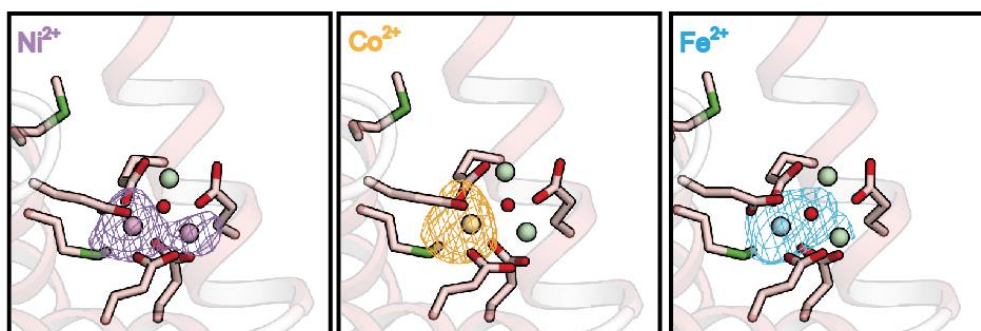


**Figure 3.17 Anomalous signal of nickel, cobalt and iron ion**

Close-up view of the anomalous difference density of nickel, cobalt and iron ions (contoured at  $3.5 \sigma$ ) are shown as a purple, orange and blue mesh, respectively.

metal ions, including ferrous ion and cobalt ion. To investigate the functional role of the MBD, I performed mutation analysis. Single or combinatorial mutations of the methionine residues (Met149 and the adjacent Met150) or the glutamate residues (Glu102, Glu105, Glu113, Glu116 and Glu153) significantly decreased the complementation activity of the growth-inhibition phenotype of *ccc1Δ* in the yeast complementation assay (Figure 3.18). Furthermore, mutants of the above two methionine residues

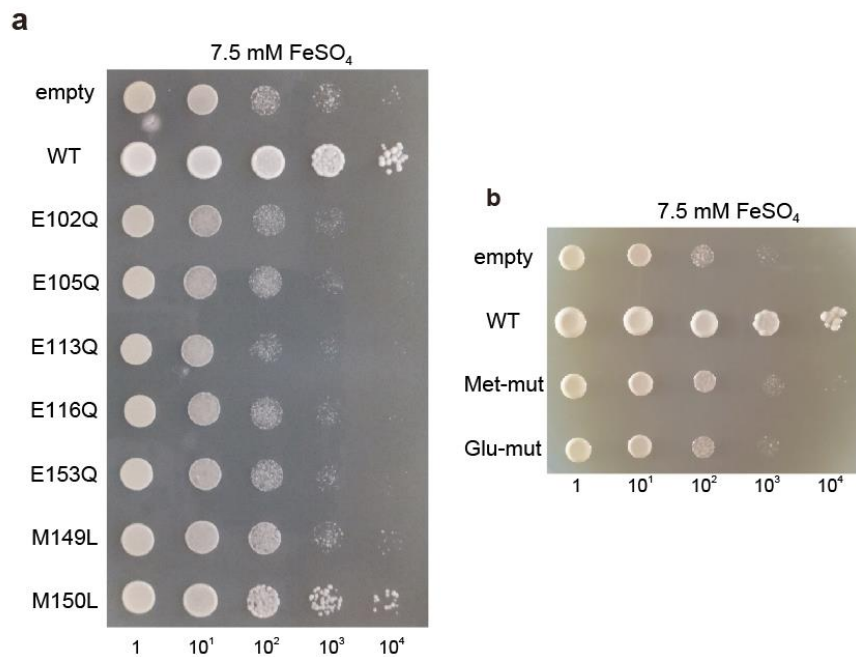


**Figure 3.18 Spot assay of mutants of the cytoplasmic metal binding site**

Functional analysis of the point mutants, the Met double mutant (Met-mut: Met149Leu and Met150Leu) and the Glu five-fold mutant (Glu-mut: Glu102Gln, Glu105Gln, Glu113Gln, Glu116Gln and Glu153Gln), assessed by a yeast spot assay

(Met-mut) or five glutamater esidues (Glu-mut) decreased the transport activity in the liposome assay (Figure 3.19). I also measured the Fe<sup>2+</sup>-uptake activity in the presence of

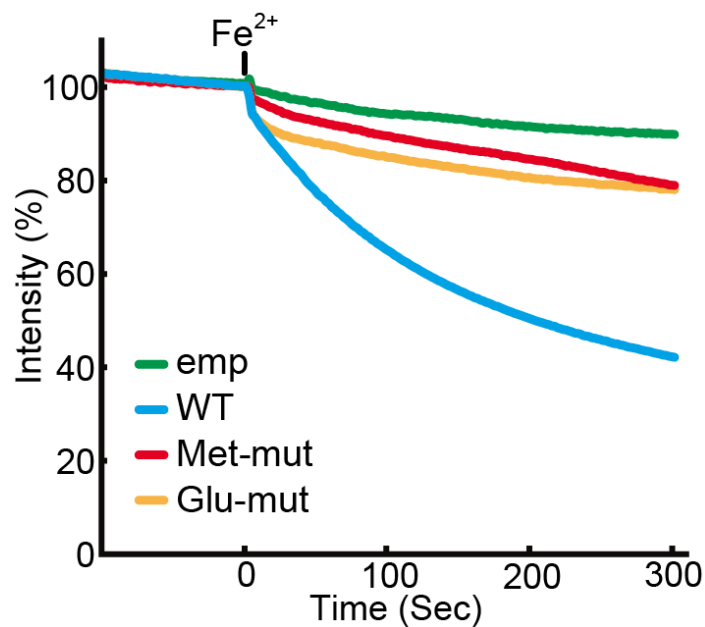


**Figure 3.19 Liposomal assay of mutants of the cytoplasmic metal binding site**

Liposomal assay of the Met double mutant (Met-mut: Met149Leu and Met150Leu) and the Glu five-fold mutant (Glu-mut: Glu102Gln, Glu105Gln, Glu113Gln, Glu116Gln and Glu153Gln). These measurements were performed with the intra- and extraliposomal pH at 7.0 and 8.0, respectively.

Zn<sup>2+</sup> and confirmed its inhibitory effect on the Fe<sup>2+</sup> transport activity (Figure 3.20). While

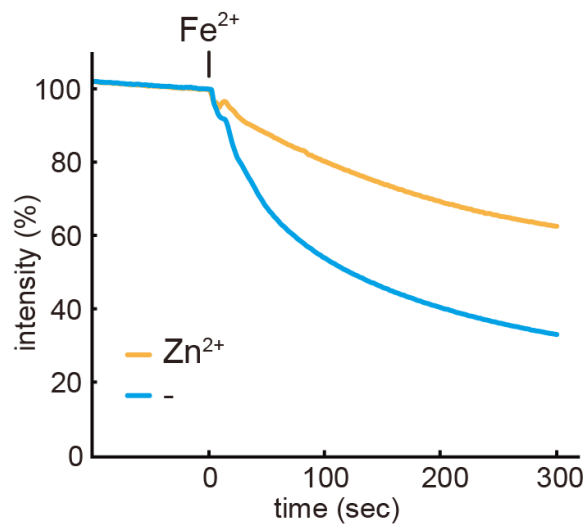


**Figure 3.20 Competition of zinc ion**

Zn<sup>2+</sup>-competition assay for EgVIT1. Binding of Zn<sup>2+</sup> to the MBD inhibits Fe<sup>2+</sup> transport activity.

the MBD is apart from the TMD, several hydrophilic and carboxylate residues are located along the cytoplasmic surface between the two domains (Figure 3.21a), and they are conserved among the VIT1 transporters (Alignment). Especially, the mutation of both Glu32 and Asp36 decreased the transport activity in liposomal assay (Figure 3.21b).

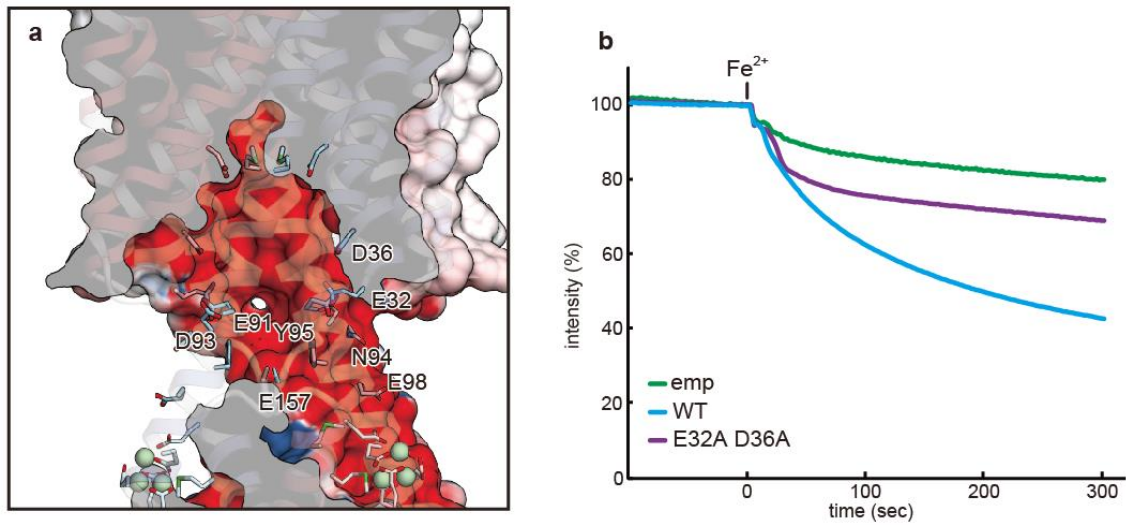


**Figure 3.21 Ion translocation from the MBD to TMD**

(a) Electrostatic surface representation along the cytoplasmic domain is shown. Protein surface from MBD and TMD is rendered electronegative by several negatively charged residues. Zinc ions captured in the crystal structure are represented by green spheres, and the distance from the metal binding site to Glu32 is indicated. (b) Liposome assay showing the importance of Glu32 and Asp36 for the ion transport.



## Chapter 4 General discussion

### 4-1 Introduction

I determined the structure of VIT1 and performed functional analysis. Those data suggest that VIT1 functions as the  $H^+$  coupled antiporter, and both TMD and MBD are important for the metal ion transport. Based on those results, I discuss the molecular mechanism of VIT1.

### 4-2 $H^+$ coupled mechanism and metal ion recognition

Liposomal analysis suggested that the metal ion transport by EgVIT1 is dependent on  $H^+$  gradient across the membrane. When the pH value of extraliposomal solution is higher than that of intraliposomal solution, the transport activity of VIT1 is enhanced (Figure 3.4). Consistently,  $H^+$ -specific ionophore CCCP, which eases  $H^+$  gradient across the membrane, decreases the transport activity (Figure 3.5). In addition, EgVIT1 transports  $H^+$  from intraliposomal solution to extraliposomal solution (Figure 3.7). Therefore, these results indicated that EgVIT1 is the  $H^+$ -coupled metal ion antiporter. The vacuolar concentration of various heavy metal ions, including iron ion, is higher than that of cytoplasmic solution, and thus transporting metal ions into vacuole requires a driving force in terms of free energy. As the pH value of vacuole maintains around 5.0 (ref. <sup>44</sup>), the  $H^+$ -coupled antiporter mechanism of EgVIT1 is proper for the cytoplasmic and vacuolar environmental differences. The hydrophilic pocket at TMD is composed of four acidic residues (Asp43 and Glu72 from each protomer). These point mutants decrease the  $H^+$  transport (Figure 3.12), indicating that they may be related to  $H^+$ -coupling during the transport. While Glu72 is still about 6 Å apart from the bound  $Co^{2+}$  and not

involved in the direct coordination (Figure 3.10), suggesting that the substrate metal ions are likely to be transported in a “relay” manner by these residues. In the current crystal structure, the carboxylate sidechains of Glu72 from the two protomers exist within about 3.7 Å (Figure 3.10). The calculated pKa value by the program PROPKA<sup>45</sup> suggest its protonation in the neutral pH condition (I crystalized EgVIT1, using HEPES-NaOH pH7.0 buffer), while Asp43 is likely to be in the deprotonated form (the pKa values of Asp43 and Glu72 are 5.9 and 8.7, respectively). Therefore, transport of the substrate metal ion would involve displacement of the proton(s) from Glu72 to Asp43. The metal ion release should involve the re-protonation of Glu72, because these carboxylate sidechains cannot reside in close proximity without protonation or cation binding. Therefore, along with the metal ion transport, one or more protons are likely to be transported from the vacuole to the cytoplasm.

According to the Lewis acid/base theory<sup>46</sup>, transition metal ions, including  $\text{Fe}^{2+}$ , are categorized as “borderline acids”, with properties in between “hard acids” and “soft acids”, which have higher and lower charge densities, respectively. Accordingly, transition metal ions can bind to both “hard bases” and “soft bases”. Recent studies reported that the substrate binding sites of the transition metal transporters DMT (also known as NRAMP) and ferroportin, which function as iron ion transporters, are composed of oxygen atoms (hard base ligands) of the carboxylate groups in aspartate and glutamate and sulfur atoms (soft base ligands) of the thioether group in methionine<sup>41,42,47</sup> (Figure 4.1). While the thioether of the methionine sidechain can function as a ligand for

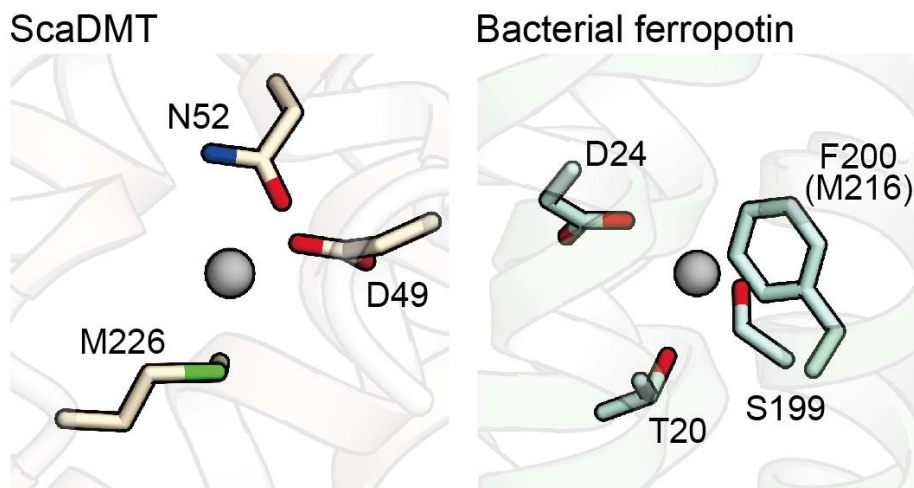


**Figure 4.1 Methionine residues of iron transporters**

Structures of ScaDMT (PDB ID: 4WGW) and bacterial ferroportin (PDB ID: 5AYW). Both structure suggested that methionine (sequence alignment show Phe residue of bacterial ferroportin is corresponded with Met residue of human ferroportin) plays a key role in coordinating iron ion.

transition metal ions, it is rather hydrophobic and not a suitable ligand for “hard acids”, such as alkaline earth metals or protons. In the transition metal ion transporter DMT, the methionine at the substrate binding site primarily contributes to the selectivity for the transition metal ions, while it concurrently discriminates alkaline earth metals, such as  $\text{Ca}^{2+}$  (ref. 48). VIT1, DMT and ferroportin recognize and transport not only iron ion but also manganese ion<sup>15,41,42</sup>. Manganese ion is also categorized as “borderline acid” as well as ferrous ion. Such molecular commonality may be attributed to the pocket composed of “hard base” and “soft base” residues. Taken together, iron ion transporters may have the similar molecular feature about the pocket. The binding site formed by “hard base” and

“soft base” residues is proper for the recognition and the release of metal ion during the transport cycle. In the current  $\text{Co}^{2+}$ -bound structure, Met80 contributes to a hydrophobic blockade from the cytoplasm solvent (Figure 4.2), which may allow the step-

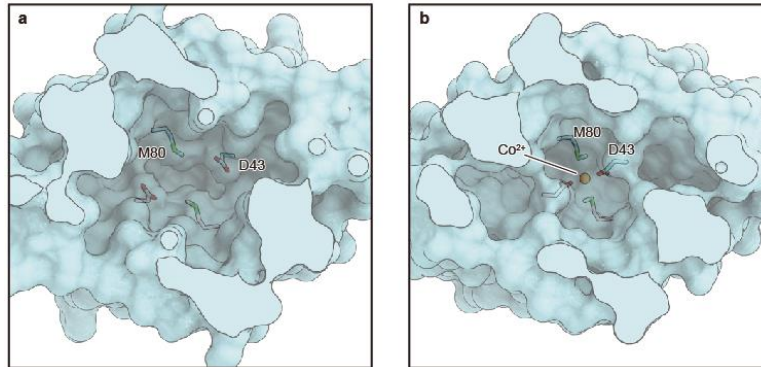


**Figure 4.2  $\text{Co}^{2+}$  binding induces partial occlusion by Met80**

(a, b) Surface representation of the cytoplasmic ion binding pocket in the non-soaked (a) and  $\text{Co}^{2+}$ -soaked (b) crystals.  $\text{Co}^{2+}$  binding induces slight inward motion of TM1 and TM2, resulting in the partial occlusion of the bound  $\text{Co}^{2+}$  ion from the cytoplasmic solvent.

by-step exchange of the substrate metal ion with the protons (Figure 4.3). The proton

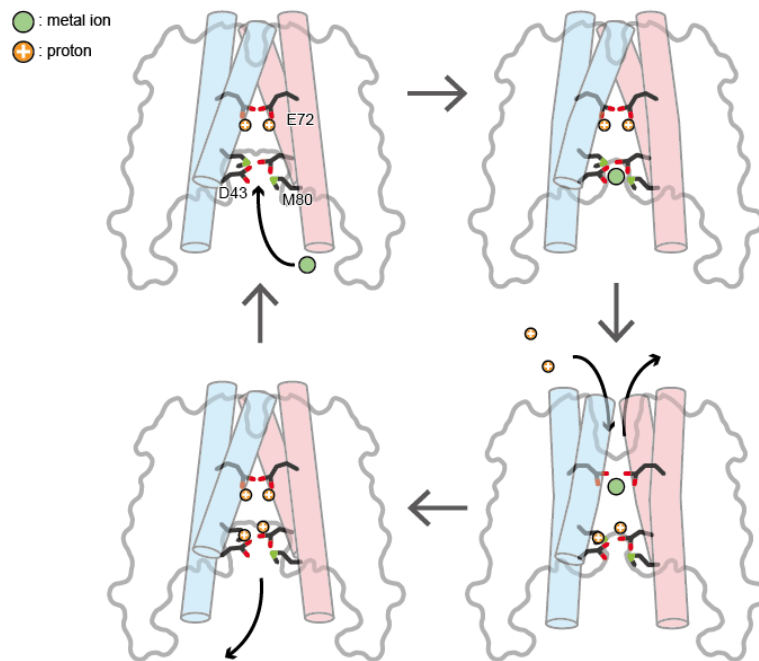


#### Figure 4.3 Iron ion transport by the hydrophilic pocket at TMD

Metal ion translocation by the TMD. Cytoplasmic metal ions are first recognized by Asp43 and Met80 and subsequently relayed to Glu72 along the central ion translocation pathway. The substrate metal ion is released to the vacuolar lumen by the kinks of TM1 and TM2, accompanied by the exchange of protons. The overall transport cycle involves the translocation of one or more protons from the vacuole to the cytoplasm.

gradient across the vacuolar membrane is especially high, as the vacuolar pH in plants and yeast is maintained at around 5 (ref. <sup>44</sup>). The “intermediate” property of the methionine sidechain should be suitable for both selective binding to the substrate metal ion and preventing proton leakage through the central ion translocation pathway.

### **4-3 Conformational change during transport**

I determine two EgVIT1<sub>23-249</sub> structures. One structure is the apo state which does not coordinate the metal ion at the hydrophilic pocket of TMD (Figure 3.8). Another structure is the Co<sup>2+</sup>-binding state (Figure 3.10). Compared to these structures, TM1 and TM2 show conformation changes by cobalt ion (Figure 3.11a). One proline and three glycine residues, which are highly conserved among VIT1 family (Alignment), contribute to these change, and their mutants decrease the transport activity (Figure 3.11b). Therefore, these residues may play key roles in the transport cycle. TM kinks at the conserved proline and glycine residues may initiate the opening of the vacuolar hydrophobic seals on the vacuolar side and thus promote the release of the substrate metal ion to the vacuolar lumen (Figure 4.3). In this study, I determine both inward-facing state and occluded state, and this conformational change of VIT1 shows the symmetric movement. Therefore, VIT1 is likely to adopt the “Rocker switch model”. However, revealing the detailed entire transport cycle requires the outward-facing state of VIT1.

### **4-4 Function of MBD**

The result of mutations of MBD indicate the critical involvement of the MBD in the metal ion transport (Figure 3.18 and Figure 3.19). Notably, the metal binding site is also composed of carboxylate groups in glutamate (hard base ligands) and sulfur atom (soft base ligands) of the thioether group in methionine, as well as the hydrophilic pocket at TMD (Figure 3.13). Fe<sup>2+</sup> is unstable in solution and easily oxidized to Fe<sup>3+</sup>, which forms insoluble salt complexes. Therefore, plants adopt various strategies to overcome this problem. For example, plant roots transport mugineic acid family phytosiderophores (MAs) into soils to chelate and form soluble iron-MA complexes for iron uptake<sup>12</sup>. For

long distance iron transport, iron in the forms of  $\text{Fe}^{3+}$  or  $\text{Fe}^{2+}$  is chelated by organic acids, such as citrate<sup>13</sup>. In this context, VIT1 transporters may utilize the MBD for capturing and accepting cytoplasmic free and/or chelating  $\text{Fe}^{2+}$  and thus facilitate its efficient transport into the vacuoles (Figure 4.4). Consistently,  $\text{Zn}^{2+}$ - competition assay and

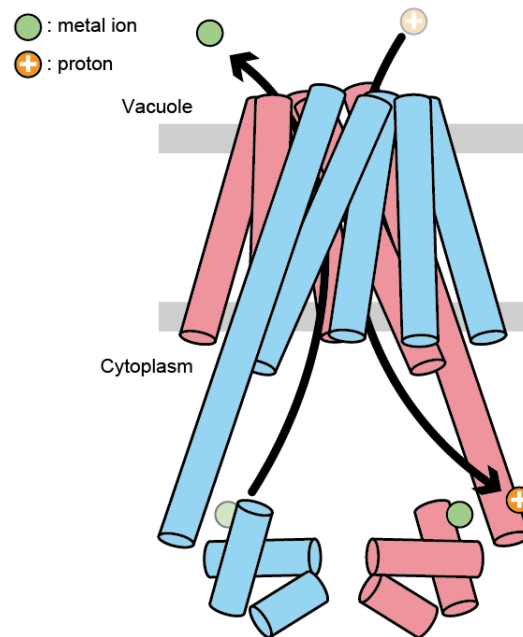


#### Figure 4.5 Putative function of MBD

The MBD and the cytoplasmic negatively charged residues facilitate substrate diffusion along the protein surface.

mutations of the two carboxylate residues (Glu32 and Asp36) located at the entrance of the ion translocating pathway decreased the  $\text{Fe}^{2+}$  transport activity in the liposome assay (Figure 3.20 and Figure 3.21), indicating especially important roles of metal binding site of MBD and these residues. Although it is also possible that the MBD has additional roles in the metal ion transport, other than a simple “facilitator”, the current hypothetical model

is in good agreement with recent bioinformatics studies, which identified VIT1-related transporters lacking an MBD<sup>24</sup> or bearing an N-terminally fused ferritin-like domain instead of the MBD<sup>25</sup> (Figure 1.7). As MbfA contains the cytoplasmic ferritin like domain which is expected to coordinate metal ions as well as MBD, MbfA may adopt a similar transport mechanism to utilize the additional domain. On the other hands, VTLs do not contain cytoplasmic additional domain. Therefore, VTLs may adopt different strategies to transport unstable transition metal ions.

#### **4-5 Conclusion**

Despite of their essential roles in all organisms, many metal ions in solution are very unstable. Therefore, all organisms have evolved specific strategies for their transport, isolation, storage and utilization. In this study, I determined the structure of plant vacuolar iron transporter VIT1, which plays the key role in vacuolar iron storage, one of the most important systems contributing to iron homeostasis in plants and yeasts. VIT1 adopts a unique transporter architecture consisting of the ion translocating TMD and the accessory cytoplasmic MBD. The cooperative function of these domains enables the efficient transport of unstable  $\text{Fe}^{2+}$  from the cytoplasm to vacuoles. The current structure and mutation analysis show the especially importance of negatively charged carboxylate residues and the thioether group of the methionine in the translocation of the transition metal ions, as well as in the metal-chelation in the accessory cytoplasmic domain. Both of these features presumably affect the *in vivo* substrate selectivity of the VIT1 transporters and thus could be candidates for modifications to design genetically modified crops. Indeed, recent research succeeded the biofortification on field growth cassava, using *Arabidopsis thaliana* VIT1 gene<sup>18,49</sup>. My work may supply this study with

information (e.g. creation of mutants which increase the transport activity). In addition to the biofortification, the current structural information may promote the design of novel anti-malaria drugs targeting the *Plasmodium* VIT1 transporter, which exports cytoplasmic Fe<sup>2+</sup> and plays an important role in the iron detoxification during the parasitism process<sup>21</sup>. Genome of all animals, including human, do not encode the VIT1 gene, suggesting that the chemical compound for VIT1 may function as the safe and efficient drug for malaria.

#### 4-6 Future perspective

I determine the structure of plant VIT1. However, our data causes a question about *Plasmodium* VIT1 and VTLs. Sequence alignment show the residues' diversity at the hydrophilic pocket of TMD. Glu72 is replaced with asparagine and glycine residues in *Plasmodium* VIT1 and VTLs, respectively (Alignment). In addition to Glu72, Y175 is also replaced with phenylalanine residue in both *Plasmodium* VIT1 and VTLs (Alignment). Especially, our analysis indicated that Y175F mutant lost the transport activity in yeast complementation assay (Figure 3.9). To understand the metal ion translocation by the pocket, we may determine structures of *Plasmodium* VIT1 and VTLs.

Overexpression of VIT1 gene increases iron ion contents in crops. As mentioned above, I speculate the candidates about the VIT1 modification. In addition to it, recent study reported that the double mutation of bacterial Na<sup>+</sup>/H<sup>+</sup> antiporter PaNhaP increases the transport activity<sup>50</sup>. This mutation induces decline in the strong interaction between residues, which contributes to change from occluded state to outward-facing state, to accelerate the transport cycle. Therefore, mutations of residues which are related to the conformational change may elevate the transport activity. In the structure of VIT1, hydrophobic residues seal the pocket from vacuolar side (Figure 3.8). The mutation of

residues (e.g. L51A, L55A, and I64A) may accelerate the iron ion transport. Such mutation strategy for plant transporters may be a good approach to modify crops, as biofortified crops improve nutrient contents to save global human health<sup>51,52,53</sup>. For these reasons, we need more structural information of plant transporters to reveal the molecular mechanism and supply the biofortification field with beneficial information.



**Table 1** Data collection and refinement statistics for *EgVIT1*<sub>90-165</sub>

	<i>EgVIT1</i> <sub>90-165</sub> (Zn <sup>2+</sup> -bound)		Ni <sup>2+</sup> -soaked		Co <sup>2+</sup> -soaked		Fe <sup>2+</sup> -soaked	
<b>Data collection</b>	BL41XU		BL41XU		BL41XU		BL41XU	
Space group	<i>P3</i> <sub>1</sub>		<i>P3</i> <sub>1</sub>		<i>P3</i> <sub>1</sub>		<i>P3</i> <sub>1</sub>	
Cell dimensions								
<i>a</i> , <i>b</i> , <i>c</i> (Å)	84.96, 84.96, 98.16		84.74, 84.74, 97.40		85.50, 85.50, 98.36		85.32, 85.32, 97.57	
$\alpha$ , $\beta$ , $\gamma$ (°)	90.0, 90.0, 120.0		90.0, 90.0, 120.0		90.0, 90.0, 120.0		90.0, 90.0, 120.0	
	peak	low- energy remote	peak	low- energy remote	peak	low- energy remote	peak	low- energy remote
Wavelength (Å)	1.282	1.300	1.485	1.522	1.6050	1.648	1.740	1.792
Resolution (Å)	50-2.25 (2.33-2.25)	50-2.25 (2.33- 2.25)	50-2.9 (3.00-2.9)	50-2.9 (3.00-2.9)	50-2.7 (2.80-2.70)	50-2.7 (2.80- 2.70)	50-3.0 (3.11-3.00)	50-3.0 (3.11- 3.00)
<i>R</i> <sub>meas</sub>	0.141 (1.425)	0.116 (1.005)	0.140 (0.340)	0.132 (0.675)	0.117 (0.794)	0.109 (0.832)	0.236 (4.512)	0.113 (1.086)
<i>CC</i> <sub>1/2</sub>	0.990 (0.241)	0.993 (0.369)	0.980 (0.791)	0.986 (0.520)	0.997 (0.743)	0.998 (0.719)	0.970 (0.048)	98.5 (0.156)
<i>I</i> / $\sigma$ <i>I</i>	3.9 (0.7)	5.7 (0.7)	5.4 (2.4)	6.1 (1.0)	14.7 (1.9)	16.0 (2.2)	4.2 (1.1)	5.0 (0.6)
Completeness (%)	96.5 (98.7)	97.5 (97.5)	99.1 (97.9)	96.7 (98.4)	100 (100)	100 (100)	98.6 (97.4)	96.0 (98.5)
Redundancy	2.1 (1.9)	2.5 (2.2)	2.6 (2.6)	2.6 (2.6)	10.2 (10.5)	10.1 (10.2)	2.6 (2.5)	2.6 (2.6)
<b>Refinement</b>								
Resolution (Å)	50-2.25 (2.33-2.25)		40.58-2.9 (3.00-2.90)		19.72-2.70 (2.80-2.25)		42.67-3.0 (3.11-3.00)	
No. reflections	37574 (3754)		17346 (798)		22018 (2200)		15090 (1437)	
Twin operator			<i>k</i> , <i>h</i> , <i>-l</i>		<i>k</i> , <i>h</i> , <i>-l</i>		<i>k</i> , <i>h</i> , <i>-l</i>	
Twin fraction			0.247		0.390		0.436	

$R_{\text{work}} / R_{\text{free}}$	19.11/24.54 (25.2/28.5)	14.48/21.13 (22.3/30.3)	15.82/21.47 (25.9/42.6)	19.16/26.49 (47.6/63.6)
No. atoms				
Protein	4716	4716	4716	4716
Water/Ion/Lipid	247	42	41	35
<i>B</i> -factors				
Protein	54.40	71.72	71.29	100.6
Water/Ion/Lipid	51.98	66.05	62.48	89.1
R.m.s deviations				
Bond lengths (Å)	0.008	0.010	0.007	0.006
Bond angles (°)	1.54	1.75	1.58	1.46
Ramachandran plot				
Favoured (%)	98.24	94.38	92.97	97.01
Allowed (%)	1.76	5.27	6.850	2.81
Disallowed (%)	0	0.35	0.18	0.18

\*Values in parentheses are for highest-resolution shell.

\*Anomalous pairs are kept separately in the merging statistics.



**Table 2** Data collection and refinement statistics for *EgVIT1*<sub>23-249</sub>

	<i>EgVIT1</i> <sub>23-249</sub>	<i>EgVIT1</i> <sub>G242C</sub>	<i>EgVIT1</i> <sub>23-249</sub> Co <sup>2+</sup> soaked
<b>Data collection</b>	BL32XU	BL32XU	BL32XU
Space group	C222 <sub>1</sub>	C222 <sub>1</sub>	C222 <sub>1</sub>
Number of crystals	5	6	7
Cell dimensions			
<i>a</i> , <i>b</i> , <i>c</i> (Å)	46.9, 290.2, 45.8	47.4, 291.1, 45.4	46.8, 290.7, 45.6
$\alpha$ , $\beta$ , $\gamma$ (°)	90.0, 90.0, 90.0	90.0, 90.0, 90.0	90.0, 90.0, 90.0
Wavelength	1.0000	1.0000	1.2800
Resolution (Å)	46.3-2.70 (2.79-2.70)	48.3-3.00 (3.11-3.00)	43.6-3.5 (3.63-3.5)
<i>R</i> <sub>meas</sub>	0.118 (1.43)	0.163 (1.054)	0.557 (1.689)
<i>CC</i> <sub>1/2</sub>	0.997 (0.794)	0.999 (0.914)	0.96 (0.423)
<i>I</i> / $\sigma$ <i>I</i>	10.6 (1.1)	12.1 (2.8)	2.85 (0.87)
Completeness (%)	99.3 (99.2)	100 (100)	99.0 (98.5)
Redundancy	6.9 (7.1)	15.5 (14.5)	6.0 (6.0)
<b>Refinement</b>			
Resolution (Å)	46.9-2.70 (2.79-2.70)		43.6-3.5 (3.63-3.5)
No. reflections	16512 (1626)		25492 (2421)
<i>R</i> <sub>work</sub> / <i>R</i> <sub>free</sub>	0.277/0.305 (0.325/0.417)		0.331/0.345 (0.378/0.392)
No. atoms			
Protein	1531		1466
Ion/Lipid	25		4
<i>B</i> -factors			
Protein	113.6		78.5
Ion/Lipid	141.5		189.0
R.m.s deviations			
Bond lengths (Å)	0.009		0.004
Bond angles (°)	0.99		1.13

---

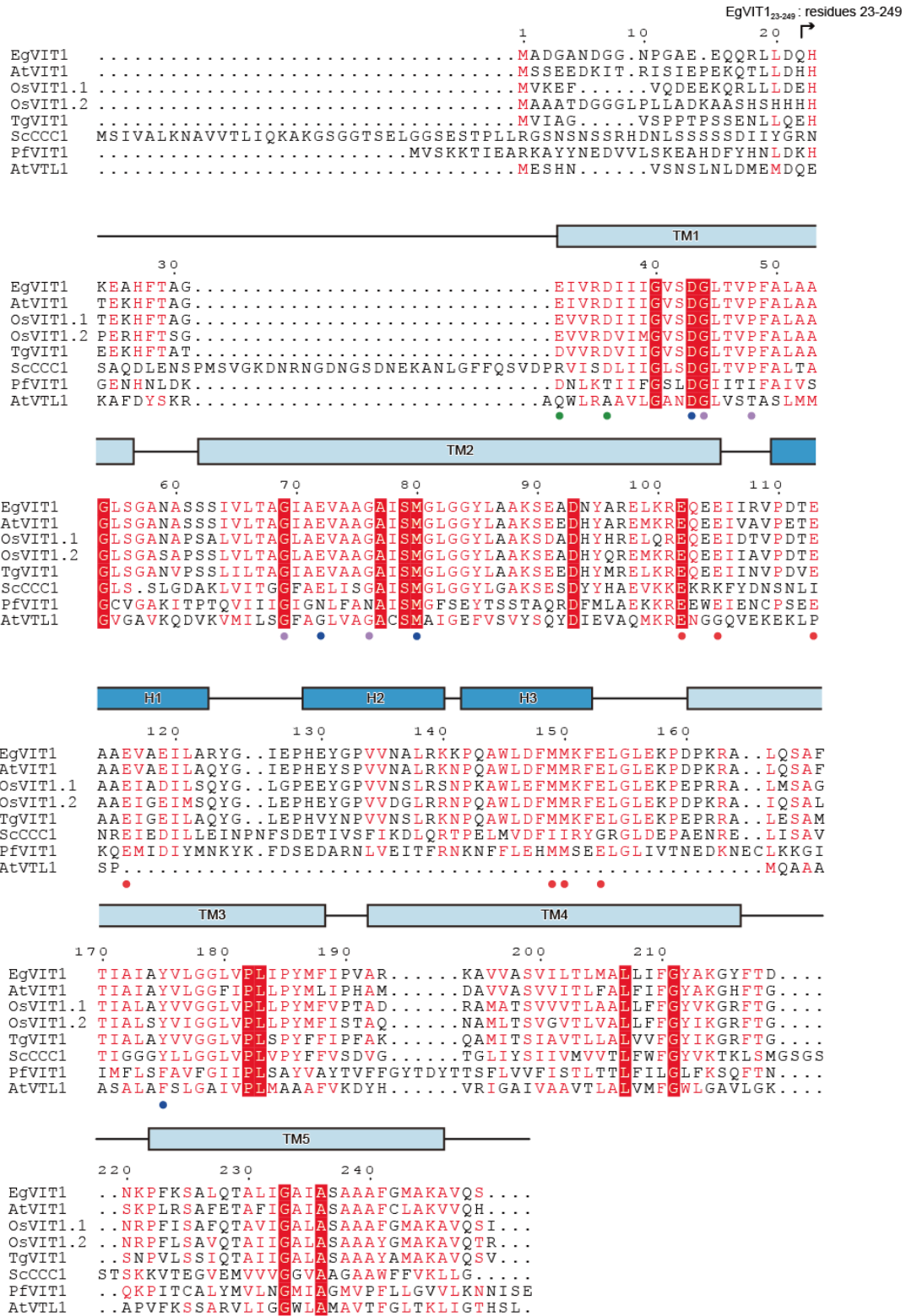
Ramachandran plot		
Favored (%)	96.0	96.9
Allowed (%)	4.0	3.1
Disallowed (%)	0	0

---

\*Values in parentheses are for highest-resolution shell.



# Alignment



### **Multiple amino acid sequence alignment of VIT1.**

Sequence alignment of *Eucalyptus grandis* VIT1 (EgVIT1 [accession number: XP\_010066557.1]), *Arabidopsis thaliana* VIT1 (AtVIT1 [OAP07733.1]), *Oryza sativa* VIT1.1 (OsVIT1 [LOC\_Os04g38940.1]) and VIT1.2 (OsVIT1.2 [LOC\_Os09g23300.1]), *Tulipa gesneriana* VIT1 (TgVIT1 [BAH98154.1]), *Saccharomyces cerevisiae* CCC1 (ScCCC1 [AAA62622.1]), *Plasmodium falciparum* VIT1 (PfVIT1 [PKC48456.1]) and *Arabidopsis thaliana* Vacuolar Iron Transporter-Like1 (AtVTL1 [AEE30069.1]). The secondary structure of EgVIT1 is indicated above the sequence. The  $\alpha$ -helices are indicated by cylinders, and TMD and MBD are colored light and dark blue, respectively. Strictly conserved residues among the CCC1/VIT1 family members and VTL1 are highlighted in red boxes, and highly conserved residues are indicated by red letters. The red, blue, purple, and green circles indicate residues involved in ion binding at the MBD, the ion translocation pathway in the TMD, kink-induction, and the ion translocation from the MBD to TMD, respectively.





## Reference

1. O., J. Simple allosteric model for membrane pumps. *Nature* **211**, 969–970 (1966).
2. Drew, D. & Boudker, O. Shared Molecular Mechanisms of Membrane Transporters. *Annu. Rev. Biochem.* **85**, 543–572 (2016).
3. Beinert, Holm & Münck; Iron-sulfur clusters: nature's modular, multipurpose structures. *Science (80-. ).* **277**, 653 (1997).
4. Balk, J. & Schaedler, T. A. Iron cofactor assembly in plants. *Annu. Rev. Plant Biol.* **65**, 125–153 (2014).
5. Zhang, C. Essential functions of iron-requiring proteins in DNA replication, repair and cell cycle control. *Protein Cell* **5**, 750–760 (2014).
6. White, M. F. & Dillingham, M. S. Iron-sulphur clusters in nucleic acid processing enzymes. *Curr. Opin. Struct. Biol.* **22**, 94–100 (2012).
7. Rouault, T. A. Mammalian iron-sulphur proteins: Novel insights into biogenesis and function. *Nat. Rev. Mol. Cell Biol.* **16**, 45–55 (2015).
8. Aust, S. D., Morehouse, L. A. & Thomas, C. E. Role of metals in oxygen radical reactions. *J. Free Radicals Biol. Med.* **1**, 3–25 (1985).
9. Bogdan, A. R., Miyazawa, M., Hashimoto, K. & Tsuji, Y. Regulators of Iron homeostasis: new players in metabolism, cell death, and disease. *Trends Biochem. Sci.* **41**, 274–286 (2016).
10. Ward, D. M. & Kaplan, J. Ferroportin-mediated iron transport: Expression and regulation. *Biochim. Biophys. Acta - Mol. Cell Res.* **1823**, 1426–1433 (2012).
11. Curie, C. *et al.* Metal movement within the plant: contribution of nicotianamine and yellow stripe 1-like transporters. *Ann. Bot.* **103**, 1–11 (2009).

12. Hider, R. C. & Kong, X. Chemistry and biology of siderophores. *Nat. Prod. Rep.* **27**, 637 (2010).
13. Ana Álvarez-Fernández, Pablo Díaz-Benito, Anunciación Abadía, A.-F. L.-M. and J. A. Metal species involved in long distance metal transport in plants. *Front. Plant Sci.* **5**, 105 (2014).
14. Sharma, S. S., Dietz, K. & Mimura, T. Vacuolar compartmentalization as indispensable component of heavy metal detoxification in plants. 1112–1126 (2016). doi:10.1111/pce.12706
15. Kim, S. A. *et al.* Localization of iron in Arabidopsis seed requires the vacuolar membrane transporter VIT1. *Science* **314**, 1295–8 (2006).
16. Zhang, Y., Xu, Y., Yi, H. & Gong, J. Vacuolar membrane transporters OsVIT1 and OsVIT2 modulate iron translocation between flag leaves and seeds in rice. *Plant J.* **72**, 400–10 (2012).
17. Momonoi, K. *et al.* A vacuolar iron transporter in tulip, TgVit1, is responsible for blue coloration in petal cells through iron accumulation. **5**, 437–447 (2009).
18. Narayanan, N. *et al.* Overexpression of Arabidopsis VIT1 increases accumulation of iron in cassava roots and stems. *Plant Sci.* **240**, 170–181 (2015).
19. Connorton, J. M. *et al.* Wheat vacuolar iron transporter TaVIT2 transports Fe and Mn and is effective for biofortification. *Plant Physiol.* **174**, 2434–2444 (2017).
20. De Steur, H. *et al.* Status and market potential of transgenic biofortified crops. *Nat. Biotechnol.* **33**, 25–29 (2015).
21. Slavic, K. *et al.* A vacuolar iron-transporter homologue acts as a detoxifier in Plasmodium. *Nat. Commun.* **7**, 10403 (2016).
22. John R. Giudicessi, BA. Michael J. Ackerman., 2013. Antimalarial drug resistance:

- a review of the biology and strategies to delay emergence and spread. *Bone* **23**, 1–7 (2008).
23. Weiner, J. & Kooij, T. Phylogenetic profiles of all membrane transport proteins of the malaria parasite highlight new drug targets. *Microb. Cell* **3**, 511–521 (2016).
  24. Gollhofer, J., Timofeev, R., Lan, P., Schmidt, W. & Buckhout, T. J. Vacuolar-iron-transporter1-like proteins mediate iron homeostasis in arabidopsis. *PLoS One* **9**, 1–8 (2014).
  25. Bhubhanil, S. *et al.* Roles of *Agrobacterium tumefaciens* membrane-bound ferritin (MbfA) in iron transport and resistance to iron under acidic conditions. *Microbiology* **160**, 863–871 (2014).
  26. Labarbuta, P. *et al.* Recombinant vacuolar iron transporter family homologue PfVIT from human malaria-causing *Plasmodium falciparum* is a Fe<sup>2+</sup>/H<sup>+</sup> exchanger. *Sci. Rep.* **7**, 1–10 (2017).
  27. Brachmann, C. B. *et al.* Designer deletion strains derived from *Saccharomyces cerevisiae* S288C: A useful set of strains and plasmids for PCR-mediated gene disruption and other applications. *Yeast* **14**, 115–132 (1998).
  28. Caffrey, M. Crystallizing membrane proteins for structure determination: use of lipidic mesophases. *Annu. Rev. Biophys.* **38**, 29–51 (2009).
  29. Hirata, K. *et al.* Zoo: An automatic data-collection system for high-throughput structure analysis in protein microcrystallography. *Acta Crystallogr. Sect. D Struct. Biol.* **75**, 138–150 (2019).
  30. Kabsch, W. Xds. *Acta Crystallogr. Sect. D Biol. Crystallogr.* **66**, 125–132 (2010).

31. Yamashita, K., Hirata, K. & Yamamoto, M. KAMO: towards automated data processing for microcrystals. *Acta Crystallogr. Sect. D Struct. Biol.* **74**, 441–449 (2018).
32. Foadi, J. *et al.* Clustering procedures for the optimal selection of data sets from multiple crystals in macromolecular crystallography. *Acta Crystallogr. Sect. D Biol. Crystallogr.* **69**, 1617–1632 (2013).
33. Schneider, T. R. & Sheldrick, G. M. Substructure solution with SHELXD. *Acta Crystallogr. Sect. D Biol. Crystallogr.* **58**, 1772–1779 (2002).
34. De La Fortelle, E. & Bricogne, G. Maximum-likelihood heavy-atom parameter refinement for multiple isomorphous replacement and multiwavelength anomalous diffraction methods. *Methods Enzymol.* **276**, 472–494 (1997).
35. Adams, P. D. *et al.* PHENIX: Building new software for automated crystallographic structure determination. *Acta Crystallogr. Sect. D Biol. Crystallogr.* **58**, 1948–1954 (2002).
36. Emsley, P., Lohkamp, B., Scott, W. G. & Cowtan, K. Features and development of Coot. *Acta Crystallogr. Sect. D Biol. Crystallogr.* **66**, 486–501 (2010).
37. Sheldrick, G. M. A short history of SHELX. *Acta Crystallogr. Sect. A Found. Crystallogr.* **64**, 112–122 (2008).
38. Thorn, A. & Sheldrick, G. M. ANODE: Anomalous and heavy-atom density calculation. *J. Appl. Crystallogr.* **44**, 1285–1287 (2011).
39. Murshudov, G. N. *et al.* REFMAC5 for the refinement of macromolecular crystal structures. *Acta Crystallogr. Sect. D Biol. Crystallogr.* **67**, 355–367 (2011).
40. Li, L., Chen, O. S., Ward, D. M. & Kaplan, J. CCC1 is a transporter that mediates vacuolar iron storage in yeast. *J. Biol. Chem.* **276**, 29515–29519 (2001).

41. Ehrnstorfer, I. A., Geertsma, E. R., Pardon, E., Steyaert, J. & Dutzler, R. Crystal structure of a SLC11 ( NRAMP ) transporter reveals the basis for transition-metal ion transport. *Nat. Struct. Mol. Biol.* **21**, 990–996 (2014).
42. Taniguchi, R. *et al.* Outward- and inward-facing structures of a putative bacterial transition-metal transporter with homology to ferroportin. *Nat. Commun.* **6**, 8545 (2015).
43. Parker, J. L., Mindell, J. A. & Newstead, S. Thermodynamic evidence for a dual transport mechanism in a POT peptide transporter. *Elife* **3**, 1–13 (2014).
44. Shen, J. *et al.* Organelle pH in the arabidopsis endomembrane system. *Mol. Plant* **6**, 1419–1437 (2013).
45. Saoudi, N., Latcu, D. G., Rinaldi, J. P. & Ricard, P. Graphical analysis of pH-dependent properties of proteins predicted using PROPKA. *Bull. Acad. Natl. Med.* **192**, 1029–1041 (2011).
46. Nieboer, E. & Richardson, D. H. S. The replacement of the nondescript term ‘heavy metals’ by a biologically and chemically significant classification of metal ions. *Environ. Pollution. Ser. B, Chem. Phys.* **1**, 3–26 (1980).
47. Ehrnstorfer, I. A., Manatschal, C., Arnold, F. M., Laederach, J. & Dutzler, R. Structural and mechanistic basis of proton-coupled metal ion transport in the SLC11/NRAMP family. *Nat. Commun.* **8**, 14033 (2017).
48. Bozzi, A. T. *et al.* Conserved methionine dictates substrate preference in Nramp-family divalent metal transporters. *Proc. Natl. Acad. Sci.* **113**, 10310–10315 (2016).
49. Narayanan, N. *et al.* Biofortification of field-grown cassava by engineering expression of an iron transporter and ferritin. *Nat. Biotechnol.* **37**, 144–151

- (2019).
50. Okazaki, K. ichi *et al.* Mechanism of the electroneutral sodium/proton antiporter PaNhaP from transition-path shooting. *Nat. Commun.* **10**, 1–10 (2019).
  51. Ruel, M. T. & Alderman, H. Nutrition-sensitive interventions and programmes: How can they help to accelerate progress in improving maternal and child nutrition? *Lancet* **382**, 536–551 (2013).
  52. De Steur, H. *et al.* Status and market potential of transgenic biofortified crops. *Nat. Biotechnol.* **33**, 25–29 (2015).
  53. Hefferon, K. L. Nutritionally enhanced food crops; progress and perspectives. *Int. J. Mol. Sci.* **16**, 3895–3914 (2015).



## Original paper

1. Takafumi Kato, Aya Kubo, Tatuya Nagayama, Shinichiro Kume, Chikara Tanaka, Yoshitaka Nakayama, Kazuko Iida and Hidetoshi Iida. Genetic analysis of the regulation of the voltage-gated calcium channel homolog Cch1 by the  $\gamma$  subunit homolog Ecm7 and cortical ER protein Scs2 in yeast. PLoS One 12 (2017).
2. Takafumi Kato, Kaoru Kumazaki, Miki Wada, Reiya Taniguchi, Takanori Nakane, Keitaro Yamashita, Kunio Hirata, Ryuichiro Ishitani, Koichi Ito, Tomohiro Nishizawa and Osamu Nureki. Crystal structure of plant vacuolar iron transporter VIT1. Nat. Plants 5, 308-315 (2019).



## **Acknowledgment**

Firstly, I would like to appreciate Professor Osamu Nureki. He always supported my study during my master's course and doctor's course. Besides him, I have been supported by many members of the Nureki laboratory. Especially, I would like to thank Dr. Tomohiro Nishizawa, Dr. Kaoru Kumazaki, Dr. Reiya Taniguchi, Dr. Yongchan Lee and Dr. Ryuichiro Ishitani. They are often strict, but they always give me accurate scientific advice and technics. In analysis of diffraction data, Dr. Takanori Nakane and Dr. Keitaro Yamashita supported me. Ms. Rieko Yamazaki, Ms. Noriko Toyama, Ms. Masayo Ogoshi, Keiko Ogomori and Sanae Okazaki, they are our laboratory's staff, supported my researching life. During my graduate school life, I enjoyed exciting and interesting experiences with Nureki laboratory's members. I would like to appreciate all of them.

When I was the undergraduate student, Dr. Hidetoshi Iida, he is the professor at the university of Tokyo gakugei, gave me many basic scientific technics. He is always gentle and encouraged me to go to the University of Tokyo. But for him, I would not have researched in Nureki laboratory. I would like to thank Prof. Iida.

In this work, a lot of collaborators supported me. Dr Kunio Hirata, he is the staff of SPring-8 BL32XU beam line, help me with measuring X-ray diffraction data. Especially, my final diffraction data were measured by ZOO system, which Dr. Hirata and Dr. Yamashita developed. Professor Koichi Ito and Dr. Miki Wada carried out yeast complementation assay. I would like to appreciate them.

Finally, I would like to appreciate my family for continuous support.

Takafumi Kato